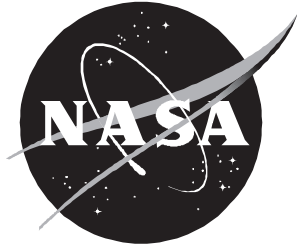


NASA/TP-2000-210555



Analysis of Post-Support and Wind-Tunnel Wall Interference on Flow Field About Subsonic High-Lift High-Speed Research Configuration

Wendy B. Lessard
Langley Research Center, Hampton, Virginia

November 2000

The NASA STI Program Office . . . in Profile

Since its founding, NASA has been dedicated to the advancement of aeronautics and space science. The NASA Scientific and Technical Information (STI) Program Office plays a key part in helping NASA maintain this important role.

The NASA STI Program Office is operated by Langley Research Center, the lead center for NASA's scientific and technical information. The NASA STI Program Office provides access to the NASA STI Database, the largest collection of aeronautical and space science STI in the world. The Program Office is also NASA's institutional mechanism for disseminating the results of its research and development activities. These results are published by NASA in the NASA STI Report Series, which includes the following report types:

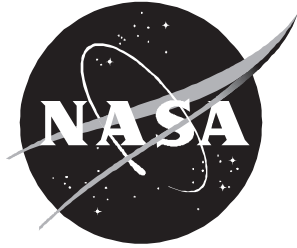
- **TECHNICAL PUBLICATION.** Reports of completed research or a major significant phase of research that present the results of NASA programs and include extensive data or theoretical analysis. Includes compilations of significant scientific and technical data and information deemed to be of continuing reference value. NASA counterpart of peer-reviewed formal professional papers, but having less stringent limitations on manuscript length and extent of graphic presentations.
- **TECHNICAL MEMORANDUM.** Scientific and technical findings that are preliminary or of specialized interest, e.g., quick release reports, working papers, and bibliographies that contain minimal annotation. Does not contain extensive analysis.
- **CONTRACTOR REPORT.** Scientific and technical findings by NASA-sponsored contractors and grantees.
- **CONFERENCE PUBLICATION.** Collected papers from scientific and technical conferences, symposia, seminars, or other meetings sponsored or co-sponsored by NASA.
- **SPECIAL PUBLICATION.** Scientific, technical, or historical information from NASA programs, projects, and missions, often concerned with subjects having substantial public interest.
- **TECHNICAL TRANSLATION.** English-language translations of foreign scientific and technical material pertinent to NASA's mission.

Specialized services that complement the STI Program Office's diverse offerings include creating custom thesauri, building customized databases, organizing and publishing research results . . . even providing videos.

For more information about the NASA STI Program Office, see the following:

- Access the NASA STI Program Home Page at <http://www.sti.nasa.gov>
- Email your question via the Internet to help@sti.nasa.gov
- Fax your question to the NASA STI Help Desk at (301) 621-0134
- Telephone the NASA STI Help Desk at (301) 621-0390
- Write to:
NASA STI Help Desk
NASA Center for AeroSpace Information
7121 Standard Drive
Hanover, MD 21076-1320

NASA/TP-2000-210555



Analysis of Post-Support and Wind-Tunnel Wall Interference on Flow Field About Subsonic High-Lift High-Speed Research Configuration

Wendy B. Lessard
Langley Research Center, Hampton, Virginia

National Aeronautics and
Space Administration

Langley Research Center
Hampton, Virginia 23681-2199

November 2000

Available from:

NASA Center for AeroSpace Information (CASI)
7121 Standard Drive
Hanover, MD 21076-1320
(301) 621-0390

National Technical Information Service (NTIS)
5285 Port Royal Road
Springfield, VA 22161-2171
(703) 605-6000

Summary

The configuration investigated in this study is the high-lift Technology Concept Airplane (TCA), which is the current baseline configuration of the High Speed Research (HSR) Program. This study investigates the effects of model supports and tunnel walls on the flow field during takeoff conditions. Experimental data were obtained at $-2^\circ \geq \alpha \geq 32^\circ$; however, this study mainly focuses on $6^\circ \geq \alpha \geq 12^\circ$, which bounds the design angle of attack (α) for takeoff. The experimental data used in this study were acquired in the Langley 14- by 22-Foot Subsonic Tunnel at a Mach number of 0.24 and a Reynolds number per inch of 1.4×10^5 . The objective of the test was to optimize the takeoff and landing performance of the configuration by varying the control surfaces. The model was instrumented with upper and lower pressure ports to measure pressure distributions that were used to aid in code calibration. In any wind-tunnel–computational-fluid-dynamics (CFD) data comparison, one must be aware of interference effects from tunnel walls, model supports, and any obtrusive hardware, which could affect the flow. Ideally, there should be minimal wall and model mount support interference so that these geometries do not have to be incorporated into the CFD simulation.

Because of the size of the support post and its potential for generating wake flow, the TCA configuration was also modeled with the post. The post support effects were not discovered while previously testing the Reference H configuration (which used the same post) because the lower pressure ports were confined only to the leading-edge part of the wing. However, the pressure field produced by the post was discovered while testing the TCA high-lift model, which had a significant number of lower surface pressures across the wing span. The experimental pressure distributions revealed a flow field characteristic of an upwash, especially in the vicinity of the post support. Thus, to accurately simulate the flow field, the post had to be modeled. To complete the CFD simulation, the tunnel walls were added to examine the interference effects of both tunnel walls and post support.

Introduction

This present investigation was undertaken in connection with the High Speed Research (HSR)

Program, which is investigating the potential benefits and trade-offs of advancements in aerodynamic efficiency, structures and materials, propulsion systems, and stability and control requirements applied to advanced supersonic cruise aircraft concepts. The configuration investigated in this study is the Technology Concept Airplane (TCA), which is the current baseline of the HSR Program. The TCA is also the second baseline configuration used in the HSR program, and postdates the initial Reference H configuration.

The present investigation deals with one important aspect of the development and testing of a supersonic transport: the need to be able to accurately predict characteristics of configurations from wind-tunnel data. In any wind-tunnel–computational-fluid-dynamics (CFD) data comparison, one must be aware of the interference effects from tunnel walls, model supports, and any other obtrusive hardware, which could affect the flow. Ideally, there should be minimal wall and model support interference so that these geometries do not have to be incorporated into the computational grid. Modeling the post mount and wind-tunnel walls is a grid-intensive, time-consuming process, and flow solver convergence problems can occur. The flow physics generated by the post can require many iterations to resolve the flow field to a steady-state condition. The present study was performed to determine how significant the effects of the model support and tunnel walls can be for an HSR configuration that was recently tested in the Langley 14- by 22-Foot Subsonic Tunnel. These modeling effects were achieved by using currently available CFD codes and then comparing the results with the wind-tunnel data. The post may contribute to an unsteady flow field depending on how the pressure field behind the post interacts with the rest of the flow. The computations performed in this study are for steady-state conditions; therefore, any deviations between experiment and computations due to flow unsteadiness cannot be accurately quantified.

This present study investigates the characteristics of the TCA takeoff configuration at a Mach number of 0.24, a Reynolds number per inch of 1.4×10^5 at design and off-design angles of attack. For efficient supersonic cruise, the aircraft must have highly swept, low-aspect-ratio wings; however, this type of configuration is typically inefficient in the subsonic flight regimes. During takeoff and landing, the flow

separates from the leading edge of the wing and a vortical flow field develops on the upper wing; this causes an increase in drag. The additional thrust required from the engines to overcome the increased drag and the low-speed performance deficiencies generates an unacceptable high level of engine noise. The environmental impact of the engine-generated noise can be minimized by reducing vortex flow separation which maximizes the takeoff lift-to-drag ratio (L/D). This is accomplished by incorporating special leading- and trailing-edge devices or attached-flow flaps onto the aircraft. The level of accurate prediction (using a validated viscous numerical method) of the subsonic flow field about an HSR model with deployed leading- and trailing-edge flaps is the main focus of this paper. As stated in reference 1, “validation is defined as the process of determining the degree to which a model is an accurate representation of the real world from the perspective of the intended uses of the model.” In validation studies, accuracy is measured with respect to experimental data.

Symbols

b	wing span, 78.24 in.
C_D	drag coefficient, $\frac{\text{Drag}}{q_\infty S}$
C_L	lift coefficient, $\frac{\text{Lift}}{q_\infty S}$
C_m	pitching-moment coefficient about $0.5\bar{c}$ (positive nose up), $\frac{\text{Pitching moment}}{q_\infty S \bar{c}}$
C_p	static pressure coefficient, $\frac{p - p_\infty}{q_\infty}$
c_l	local chord, in.
\bar{c}	mean aerodynamic chord, 56.97 in.
j_{\max}	largest grid index in j direction
j_{\min}	smallest grid index in j direction
M_∞	free-stream Mach number
p	static pressure, psi
q	dynamic pressure, psi

Re_L	Reynolds number per unit length, 1/in.
S	reference area, in ²
x, y, z	body axis coordinates, in.
x/c_l	fraction of local chord
y^+	law-of-wall coordinate, $[(\rho \tau_w)^{0.5}/\mu](Re_L/M_\infty)^{0.5} y$
$y/(b/2)_l$	fraction of local semispan
α	angle of attack, deg
δ_{LE}	leading-edge flap deflection angle (positive down), deg
δ_{TE}	trailing-edge flap deflection angle (positive down), deg
μ	molecular viscosity coefficient, lb-sec/in ²
ρ	density
τ_w	shear stress at wall

Abbreviations:

CFD	computational fluid dynamics
HSR	high-speed research
LE	leading edge
MAC	mean aerodynamic chord
MBL	model buttline
MFS	model fuselage station
MW	megaword
TCA	Technology Concept Airplane
TE	trailing edge
WL	water line

Subscript:

∞	free stream
----------	-------------

Experimental Apparatus and Model Description

The wind-tunnel data used in this study were obtained in the Langley 14- by 22-Foot Subsonic Tunnel, which is a closed-circuit, single-return atmospheric tunnel. The test section is 14.5 ft high by 21.75 ft wide and was configured with closed walls and ceiling for this test. A more detailed description of the wind tunnel is given in reference 2. The wind-tunnel data (surface pressures and force and moment data) were obtained at a nominal free-stream dynamic pressure of 0.60 psi, which produced a test Mach number of approximately 0.24 with slight variations due to temperature changes and a test Re_L of approximately 1.4×10^5 per inch.

A three-view sketch of the model is presented in figure 1. The model was equipped with simple-hinged flaps at the leading and trailing edges, which were designed to produce attached flow at design conditions. The model was composed of two leading-edge flaps, which separated at the crank when deflected. The model had two inboard trailing-edge flaps and two outboard trailing-edge flaps. The design high-lift configuration for takeoff was defined when the leading- and trailing-edge flaps were deflected at $\delta_{LE} = 30^\circ$ and $\delta_{TE} = 10^\circ$, respectively. The takeoff design configuration for the TCA is the main focus of this investigation. This study addresses the following case scenarios tested in the 14- by 22-Foot Subsonic Tunnel:

- (1) TCA wing-body without post support (free air)
- (2) TCA wing-body with post support
- (3) TCA wing-body with post support and tunnel walls

Because the model was sized for the 14- by 22-Foot Subsonic Tunnel, tunnel wall effects were expected to minimally impact the flow about the model.

Table 1 presents the geometric characteristics of the model. The wing is projected to the centerline to determine reference area. The wing thickness makes a transition from a blunt leading edge to a sharp leading edge at the planform break, which is located at 24.02 in. at the model buttline (MBL). The wind-

tunnel model makes this transition abruptly, which results in a sharp step; however, the numerical model uses a linear interpolation over a region of 0.30 in. to smooth this sharp transition region and to simplify the grid generation. The grid did not model the spaces between the leading-edge flaps when they were deflected for takeoff. The wind-tunnel model was also blended in this region with a filler material. The pressure port locations on the TCA are shown in figure 2. The upper surface ports are on the right wing, and the lower ports are on the left wing. The experimental pressure distributions at the eight designated model fuselage stations (MFS) and six model buttline stations are used to compare with the computational results.

Table 1. Geometric Characteristics of Wing Model

Wing aspect ratio	2.027
Reference area, ft^2	21.25
Outboard LE sweep, deg	71
Inboard LE sweep, deg	52
\bar{c} , in.	56.97
Span, in.	78.24
Model length, in.	195.6
Taper ratio	0.0664
Outboard break chord	MFS 122.68, MBL 24.02
50-percent MAC, in.	MFS 115.24
Tip chord, in.	5.11

A photograph of the model mounted in the Langley 14- by 22-Foot Subsonic Tunnel is shown in figure 3. The model is a 5-percent scale-down version of the full-scale high-lift TCA configuration. The model was mounted on a post, which had a pitching mechanism to allow for different angle-of-attack conditions. The drawings shown in figure 4 show the dowel pin assembly used to attach the post to the internal balance. The location of the pitch mechanism or link is also labeled in the figure. A six-component strain-gauge internal balance measured the forces and moments. A spring-loaded sliding seal was fitted to the inside of the model to minimize the opening around the post support. The model and post support assembly were mounted on a turntable which provided for sideslip variation. Corrections were applied to the free-stream dynamic pressure to account for model and support system blockage. Corrections were also applied to model force and moment data to remove the effects of the tunnel walls, post support system, and flow angularity. Grit was used on the forebody to force transition of fuselage boundary layer. There was

no guarantee that the flow over the wing was turbulent, and no grit was applied to the wing. An assumption that the entire flow field was turbulent was made in the calculations.

Computational Grids

The grids used in this study were provided by the Langley Geometry Laboratory (GEOLAB). Each grid was generated in several stages. First the Initial Graphics Exchange Specification (IGES) data were read into the Integrated Computer-Aided Engineering and Manufacturing (ICEM) (ref. 3) software system where the grid block topology is set up and the coarse Euler volume grids are generated. The block faces are then refined by GRIDGEN2D (ref. 4) (an interactive software program used to generate grids) to ensure smoothness and orthogonality. Additional grid points are distributed in the boundary layer to satisfy the viscous spacing requirements, and the volume grids are generated accordingly.

The MultiGeometry Grid Embedder (MaGGiE) code (ref. 5) is used to determine the interpolation information between grids. The grids for the post support and tunnel walls were generated with a hyperbolic grid generator (HYPGEN) (ref. 6). The HYPGEN program is used to generate a three-dimensional volume hyperbolic grid over a known single-block surface grid by using the three-dimensional hyperbolic equations. In order to incorporate the post support and tunnel walls in the calculations, the chimera technique was used, which allows grids with different topologies to overset each other.

The surface and volume grids of the 5-percent scale high-lift TCA free-air configuration were generated first. The surface grid plotted with the symmetry plane is shown in figure 5. The model used for the surface grid was composed of the wing-body only, neither empennage nor nacelles were included. The forebody has a C-O topology and the wing and wake regions have a C-H topology. The grid is composed of 26 blocks, 53 point-to-point matching interfaces, and 3 patched boundaries. The entire volume grid contains over 6×10^6 points. A blocking arrangement was used similar to the one on the Reference H configuration (ref. 7). This blocking strategy maintained point-to-point continuity across grid boundaries and simplified

the boundary condition setup for the trailing-edge flaps.

The grid for the TCA with the post was generated by inserting the post grid into the free-air grid by using the chimera technique. Three angle-of-attack conditions were investigated, and for each case a separate grid was generated. To ease the grid generation process, the post was rotated counterclockwise to $\alpha = 6^\circ$, 8° , and 10° before it was inserted into the free-air grid. The model was pitched up to be properly aligned with the post for each angle of attack. The rotation was specified in the CFL3D's input file as the angle-of-attack condition; this rotated the model and post to their respective positive angles of attack. This multiblock grid contained 28 blocks with the post. A global view of the TCA configuration mounted on the post is shown in figure 6, and the grid contained about 6.5×10^6 points.

The post support is surrounded by an intermediate block, which has a grid distribution comparable with the surrounding global grid to facilitate interpolation of the overset region. Because the walls were not being modeled in this particular case, the post needed to be extended out into the far-field grid and gradually tapered off to a singularity line to minimize any interference effects in surrounding flow field. Essentially, the post geometry for this particular grid was simulated up to the forward-facing step (fig. 4). The grid did not model the indentation on the backside of the post where the pitch link was inserted. Below the step, the conical shape of the post was flattened until it gradually became a line at the symmetry plane. (See fig. 7.) The post grid interfaces with the lower fuselage, intermediate grid, and surrounding volume grid and is shown in figure 8. The circles represent the intermediate grid, the asterisks represent the post grid, and the grid lines shown in the symmetry plane represent the surrounding volume grid. The grid lines adjacent to the lower wing (shown as a shaded surface in fig. 8) are part of the lower wing-fuselage surface and was not shaded so that the overlapping of the grid lines would clearly be seen.

The next grid that was generated modeled the wind-tunnel walls in addition to the post support. A Cartesian wind-tunnel grid was generated in place of the far-field boundary, and the grids of the model and post were overset onto this domain. The holes

generated in the volume grid by the chimera scheme are shown in figure 9 (which plots every other grid point), which depicts where the grid points have been blanked out around the model and post support. Unlike the previous volume grid, which had a comparable grid distribution to the intermediate grid, the Cartesian wind-tunnel grid varied more in cell size, aspect ratio, and orientation with respect to the intermediate grid, which surrounded the post. The differences in these block topologies made the chimera interpolation more challenging, and the gridding around this area (wind-tunnel wall, intermediate grid, and post) had to be redistributed several times before the resulting interpolation values were within the specified tolerances. A detailed view of the overset grids for the post and wind-tunnel case is shown at the symmetry plane in figure 10. Because the wind-tunnel walls were simulated in this case, the post geometry was modeled to the correct height and diameter before it was overset onto the tunnel floor. This is shown in figure 11. The volume grid of the post support modeled in the wind tunnel contained 29 blocks and approximately 5.6×10^6 grid points.

Computational Method

The subsonic flow field about the wing-body high-lift TCA configuration was simulated with CFL3D. This code solves the Reynolds averaged, thin-layer, three-dimensional, time-dependent, compressible Navier-Stokes equations in conservation law form. More details about the computational method and the code can be found in reference 8. The interpolated coefficient values between the patched interfaces were determined by using RONNIE (ref. 9). The overset interpolated values were obtained with the code, MaGGiE.

Viscous cell spacing normal to the forebody, wing-fuselage-afterbody, and wake region was 2×10^{-6} , which is required for $y^+ = 1.0$ to accurately simulate the viscous boundary layer for turbulence. A single exponential function was used for the grid expansion in the normal direction. To minimize the total number of grid points, inviscid spacing was used at the tunnel walls and at the side of the trailing-edge flaps. The grid spacing at the side of trailing-edge flaps is $(7.3 \times 10^{-4})\bar{c}$. The far-field boundary (wind tunnel not modeled) extends approximately $5.8\bar{c}$ upstream of the fuselage, $5\bar{c}$ circumferentially away

from the centerline, and $3.7\bar{c}$ downstream of the afterbody. The conditions of no-slip and impermeability with zero normal gradient for pressure and temperature are imposed at the solid boundaries. Symmetry conditions are used along the vertical plane of symmetry for the semispan grids. One-dimensional characteristic inflow-outflow boundary conditions are used in the far field. Flow-through boundary conditions are specified between the trailing-edge flaps.

The location of flow transition on the wing was not experimentally determined and therefore unknown. Hence, as previously stated, a fully turbulent flow was assumed for all the calculations. The field equation turbulence model of Spalart and Allmaras (ref. 10) was attempted, but a converged solution was unable to be obtained. The algebraic turbulence model developed by Baldwin and Lomax (ref. 11) was used instead, and for the separated flow regions, the method of Degani and Schiff (ref. 12) was used to determine the proper length scale for the turbulence model. The turbulent viscous terms were calculated normal to the surface for the post and TCA wing-body numerical geometries. The wind-tunnel walls were modeled inviscidly.

Solution Convergence

All computations were performed on the Numerical Aerodynamic Simulation (NAS) Cray-2 computer, which is located at Ames Research Center. Solution convergence was accelerated by using three levels of multigrid on the finest mesh only. The mesh-sequencing approach could not be used for the chimera interpolation. The TCA grid in free air had approximately 6.0×10^6 points, the TCA grid with the post had 6.5×10^6 grid points, and the TCA grid with post support and wind-tunnel walls had 5.6×10^6 points. Since the far field of the grid was reduced to the tunnel dimensions, less points had to be used to define the tunnel volume grid. The memory required to run each solution ranged from approximately 250 to 280 MW. The average run rate for the CFL3D code with MaGGiE was about 12 $\mu\text{sec}/\text{iteration}/\text{cell}$. The C_L history plots at $\alpha = 8^\circ$ are shown in figure 12 for the TCA wing-body configuration in free air (fig. 12(a)), with post (fig. 12(b)), and with post and wind-tunnel walls (fig. 12(c)). As evident from figures 12(b) and (c), the post and walls introduce additional flow physics which take longer to resolve;

therefore, calculations were performed over more iterations than for the free-air case (fig. 12(a)). The oscillations occur over a larger amount of iterations once the post is introduced; this leads one to suspect that the solution did not completely converge because of some flow unsteadiness. The oscillatory behavior for the post case was expected to increase once the wind-tunnel walls were added. Because convergence could not be expected without lengthy and costly computer time, the solution for the post and tunnel walls was stopped at about 1800 iterations. The residual decreased by 3 orders of magnitude for the free-air case and 2.5 orders of magnitude for the post support and wind-tunnel wall case.

Results

Experimental forces, moments, and surface pressures are compared with computational data. The results of the wing-body TCA high-lift configuration in free air, with post, and with post and wind-tunnel walls are presented. To aid in pressure contour clarification, the upper and lower surfaces of the TCA are shown in gray-scale, and the contour lines are labeled to provide detailed quantitative information. Surface streamlines and total pressure contours in the near-wake region of the model are computed and greatly contribute to the understanding of the flow physics for this high-lift TCA configuration.

The wind-tunnel test measured forces and moments for $-2^\circ \geq \alpha \geq 32^\circ$, and these curves are shown at the top of figures 13(a), (b), and (c). For this wide range of angle of attack, one can see the overall performance features of the model. The simulated free-air cases were performed at $\alpha = 6^\circ, 8^\circ, 10^\circ$, and 12° and compared with the corrected and uncorrected experimental data. These angles of attack were chosen because they bracketed the design takeoff angle (approximately 9°) for the TCA. The corrections normally applied to the tunnel data corrections appear to be valid because they bring the uncorrected tunnel data into agreement with the computed free-air case.

A close-up view ($\alpha = 4^\circ$ to 14°) of each curve for C_L , C_D , and C_m (figs. 13(a), (b), and (c), respectively) clearly shows that the corrected experimental data compare better with the computational free-air case than the uncorrected experimental data. The largest discrepancy in C_L between the corrected test data and

the computational free-air case occurs at $\alpha = 12^\circ$, a difference of approximately 0.03. Interestingly, the uncorrected and corrected test data are essentially the same value at this angle of attack. The greatest difference in C_D also occurs at $\alpha = 12^\circ$, where a difference of about 0.01 or 10 drag counts exists between the computed and corrected test value. The greatest discrepancy in C_m occurs at the lower angle of attack, $\alpha = 6^\circ$.

Obtaining measurements of surface pressures is very desirable, especially when comparing with CFD data, because it helps to validate the numerical method used. The surface pressure coefficients are calculated with the corrected q values. As shown in figures 14, 15, and 16, experimental surface pressure coefficients are presented along with the computed model results simulated in free air and with post. The post effects dramatically impact the upper and lower surface pressure distributions and show that while the forces and moments may be reasonably predicted, the flow physics are not being correctly captured. As expected, the greatest post effects are seen in this vicinity of the post.

A few of the more noteworthy stations are examined. A very obvious effect of the post is seen on the top and bottom of the TCA surface, at $x = 112.0, 120.0$, and 125.5 in.; this is clearly seen in figures 14(a), 15(a), and 16(a), respectively. In the streamwise direction, the stations at $y = 6.0$ and 15.0 in. (figs. 14(b), 15(b), and 16(b)) show the large effect the post has on the pressure coefficient distributions. At $\alpha = 10^\circ$, a relatively large suction peak is noted at $x = 100.5$ at approximately 80 percent span and propagates downstream. This vortex, which is greater in magnitude than the ones formed at $\alpha = 6^\circ$ and 10° , continues to propagate downstream; this suggests that the upwash from the pressure field created by the post is increasing with angle of attack.

The post produces an increase in pressure on the inboard lower surface of the wing ahead of the post. At and behind the post, the pressure on the lower wing surface is reduced. This reduction results in decreased flow circulation about the wing because the pressure increments between the upper and lower wing surfaces are less. The effect of the post can also be seen in the off-surface w -component of velocity plotted in figures 17(a) and (b) at $x = 115$ in. for the free-air and post cases, respectively. For the post case, the

w -component of velocity is slightly higher below the wing which is evidence of a slight increase in upwash. This increase in upwash causes the flow to separate sooner and a primary vortex develops further upstream when compared with the free-air case. Hence, the relative local angle of attack has increased. The exact location of the predicted vortex separation is dependent on the turbulence model used. In the calculations, the entire wing is assumed to be turbulent without any laminar boundary layer regions. If a laminar region existed during the wind-tunnel test is unknown.

The wind-tunnel walls were included in the computational simulation for one angle of attack, $\alpha = 8^\circ$, and computational spanwise and streamwise C_p distributions are compared with experiment in figure 18. Because of the time-intensive grid generation that was required for every angle of attack plus the long solution run time, no other conditions were run for the tunnel case. There are obvious wind-tunnel wall effects on the flow field. All the spanwise stations show higher suction peaks occurring for the post and tunnel wall cases partly because of a channeling effect caused by the wind-tunnel walls. The increase in upwash previously mentioned is greater in the post and wind-tunnel wall case than with the post alone. This upwash would also cause a stronger vortex to develop in the wind-tunnel case. This vortex is clearly shown in figure 18(a) for all the spanwise stations ($x = 86.5$ to 133.0 in.), which predicted higher suction peaks for the wind-tunnel case compared with the other two cases (free air and with post).

To determine how well the chimera method performed, pressure contours are plotted across the over-set regions of the grid, as shown in figure 19. At the symmetry plane ($y = 0.0$), the contours are continuous across the grid blocks in front of the post. Behind the post, the contours are less continuous, which indicates that the flow field is unsteady in the wake behind the post. The chimera interpolation at the top and bottom of the post shows a fair match among the contour lines from block to block. As previously stated, the effect of wind-tunnel walls on the model flow field was minimal as shown in figure 20. The computational pressures calculated on the wall opposite the symmetry plane as well as on the ceiling show little variation in pressure gradients. As expected, the high pressure gradients are seen on the tunnel floor near the post support. Figure 21 depicts a more detailed view of the

computational pressure coefficients on the upper surface. Figure 21(a) represents the free-air case, figure 21(b) represents the model with post, and figure 21(c) represents model with post and wind-tunnel walls. A noted difference is seen in the upper surface pressures when the post is simulated. Comparing figure 21(a) with figures 21(b) and (c) shows differences midway along the wing span. The post creates an upwash, which causes lower regions of pressure when compared with figure 21(a). As shown in figure 22, the gradient associated with the post is evident.

The upper surface streamlines generated from the computational solutions at $\alpha = 8^\circ$ are shown in figure 23 for the free air, post, and post with tunnel walls. The separation and reattachment lines for the primary and secondary vortices are labeled for clarity. The primary separation line, which cannot be seen because it is located at the leading edge of the wing, is not labeled for any case. The post and tunnel wall case show similar flow characteristics as the free-air case, and they are labeled in the figure. Basically, the main difference between the free-air case and the post cases (with and without walls) is that the post cases show a stronger primary and secondary inboard vortex.

The total pressure contours in the wake region (FS = 143 in.) for the free air and post support cases are shown in figure 24. This wake information clearly shows the impact of the post on the flow field. A larger and more expansive vortical system develops midway in the spanwise direction on the wing for the post cases. This effect is clearly evident in many of the pressure plots (figs. 14 to 18). For example, in figure 15 at $x = 100.5$ in., a vortex does not even form for the free-air case but is captured when the post is modeled. Examination of the calculated flow field (total pressure contours) for the free-air case (fig. 24(a)) shows two pairs of tightly formed vortices, which develop around the two inboard trailing-edge flaps. The post cases (figs. 24(b) and (c)) develop a less defined inboard vortical system.

The overall performance characteristics of the computational solution, such as lift, drag, and pitching moment, compare well with experimental data; this may lead one to assume that the flow field has been correctly simulated. Although the global flow features (forces and moments) for the free-air case compare

well with experiment, the flow physics are not accurately captured as evident in the pressure plot comparisons when modeling without the post. If one is trying to verify the ability of a code to predict the high-lift flow around a high-speed civil transport, more corroborating evidence is needed to determine if the numerics are predicting surface and off-body flows accurately. Until this is done, the uncertainty one has in predicting future flows for this type of configuration is truly unknown.

Concluding Remarks

The 5-percent Technology Concept Airplane (TCA) wing-body high-lift model was simulated in free air, with a post, and with a post and wind-tunnel walls. The wind-tunnel conditions were a Mach number of 0.24, and Reynolds number per inch of approximately 1.4×10^5 . Experimental results at several angles of attack were compared with the computational results obtained from a thin-layer Navier-Stokes code (CFL3D), which used the chimera technique to incorporate components with different topologies. Modeling the TCA configuration in free air proved to be sufficient in capturing the global performance characteristics of the flow field and could confidently be used for a quick assessment of the configuration for preliminary design work. The computational forces and moments compared well with experiment. Analy-

sis of the computational surface pressures clearly show that the flow physics were not being properly modeled without the post; however, once the post was inserted using the chimera technique in CFL3D, very good agreement with test pressure data occurred. Adding the wind-tunnel walls to the post case also yielded good code-to-test comparisons, and it is difficult to ascertain if modeling the walls with the post was more accurate than without the walls. This is due to the sparse placement of pressure ports on the model.

A code calibration study should account for any wind-tunnel or model support interference effects if deemed necessary. Therefore, a determination should be made early on whether the wind-tunnel walls or other protuberances in the flow need to be modeled by simulating the experimental setup with and without the potential flow obstructions. Obviously, if the model support system and/or tunnel walls only minimally affect the flow, then it may make sense to simulate the model in free air, thus reducing the time and effort spent on grid generation and on running the solution to convergence. For the prediction of overall performance such as forces and moments, modeling the TCA in free air appears to be sufficient. To capture the local flow physics, this study has shown that the post must be modeled; this is evident after comparing the computational and experimental surface pressures with and without the post.

References

1. AIAA Guide for the Verification and Validation of Computational Fluid Dynamics Simulations. AIAA G-077-1998, 1998.
2. Gentry, Garl L., Jr.; Quinto, P. Frank; Gatlin, Gregory M.; and Applin, Zachary T.: *The Langley 14- by 22-Foot Subsonic Tunnel—Description, Flow Characteristics, and Guide for Users*. NASA TP-3008, 1990.
3. Akdag, Vedat; and Wulf, Armin: Integrated Geometry and Grid Generation System for Complex Configurations. *Software Systems for Surface Modeling and Grid Generation*, Robert E. Smith, ed., NASA CP-3143, 1992, pp. 161–172.
4. Steinbrenner, John P.; and Chawner, John R.: Recent Enhancements to the Gridgen Structured Grid Generation System. *Software Systems for Surface Modeling and Grid Generation*, Robert E. Smith, ed., NASA CP-3143, 1992, pp. 253–272.
5. Lessard, Victor Robert: Domain Decomposition for Multigrid, Finite Volume Flow Solvers. MS Thesis, Old Dominion Univ., Dec. 1989.
6. Chan, William M.; Chiu, Ing-Tsau; and Buning, Pieter G.: *User's Manual for the HYPGEN Hyperbolic Grid Generator and the HGUI Graphical User Interface*. NASA TM-108791, 1993.
7. Lessard, Wendy B.: *Navier-Stokes Simulation of Several High-Lift Reference H Configurations*. NASA/TP-1999-209541, 1999.
8. Thomas, J. L.; Taylor, S. L.; and Anderson, W. K.: Navier-Stokes Computations of Vortical Flows Over Low Aspect Ratio Wings. AIAA-87-0207, 1987.
9. Biedron, R. T.; and Thomas, J. L.: A Generalized Patched-Grid Algorithm With Application to the F-18 Forebody With Actuated Control Strake. *Comput. Syst. Eng.*, vol. 1, no. 2–4, Jan. 1990, pp. 563–576.
10. Spalart, P. R.; and Allmaras, S. R.: A One-Equation Turbulence Model for Aerodynamic Flows. AIAA-92-0439, 1992.
11. Baldwin, B. S.; and Lomax, H.: Thin Layer Approximation and Algebraic Model for Separated Turbulent Flows. AIAA-78-257, 1978.
12. Degani, D.; and Schiff, L. B.: Computation of Supersonic Viscous Flows Around Pointed Bodies at Large Incidence. AIAA-83-0034, 1983.

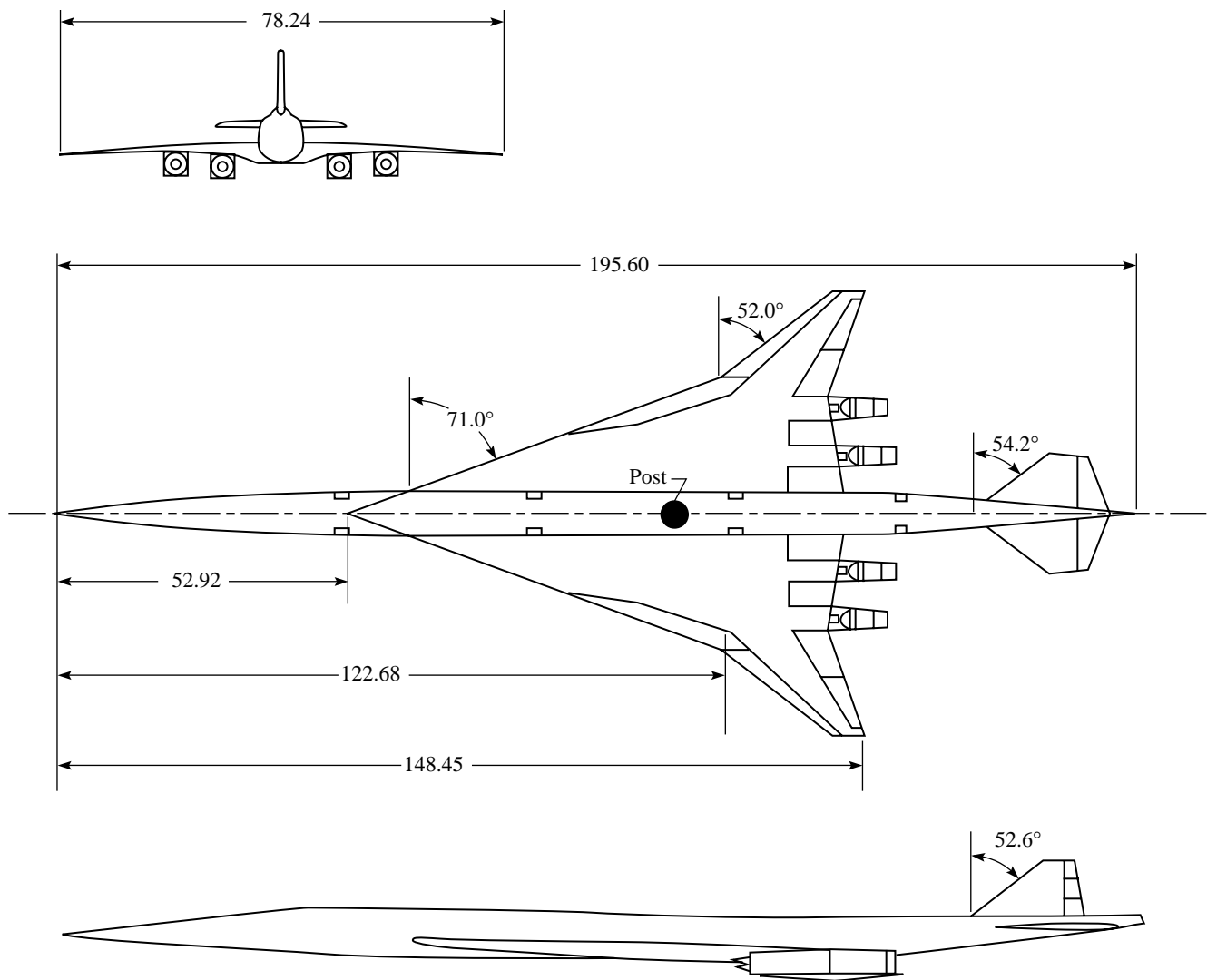


Figure 1. Three-view sketch of high-lift TCA configuration. Linear dimensions are in inches.

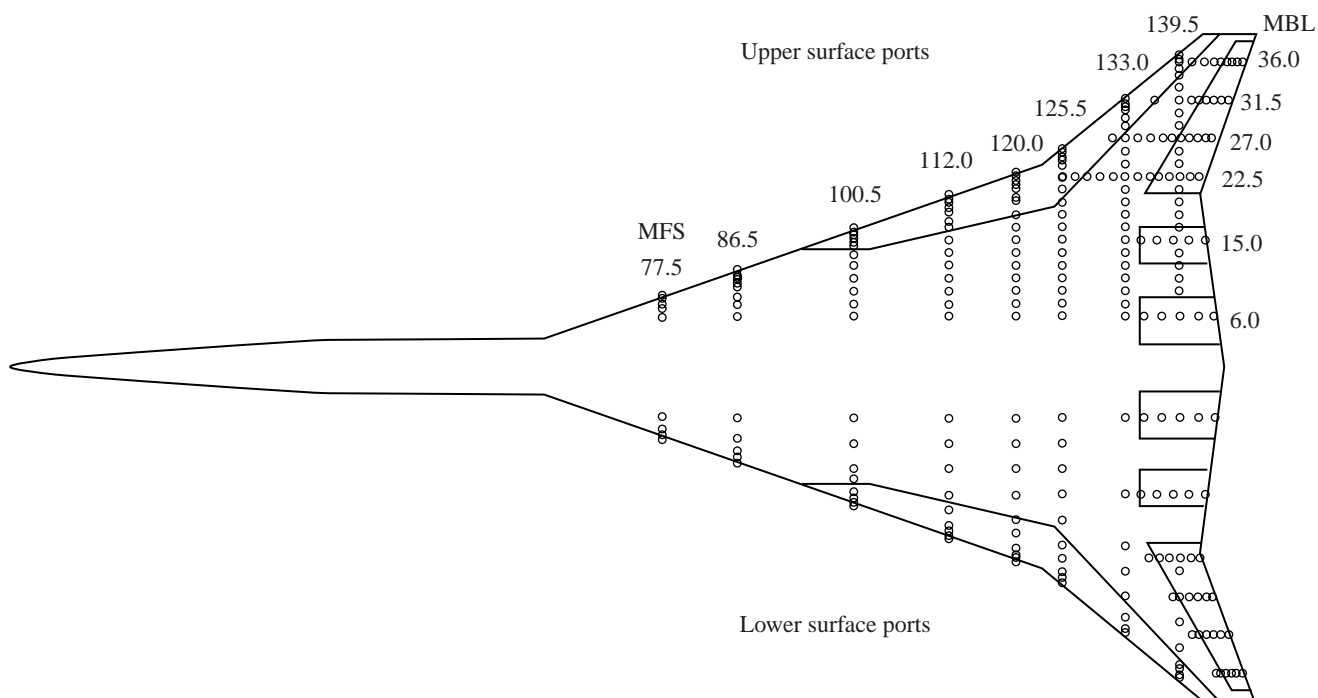


Figure 2. Pressure port locations on TCA. Dimension are in inches.

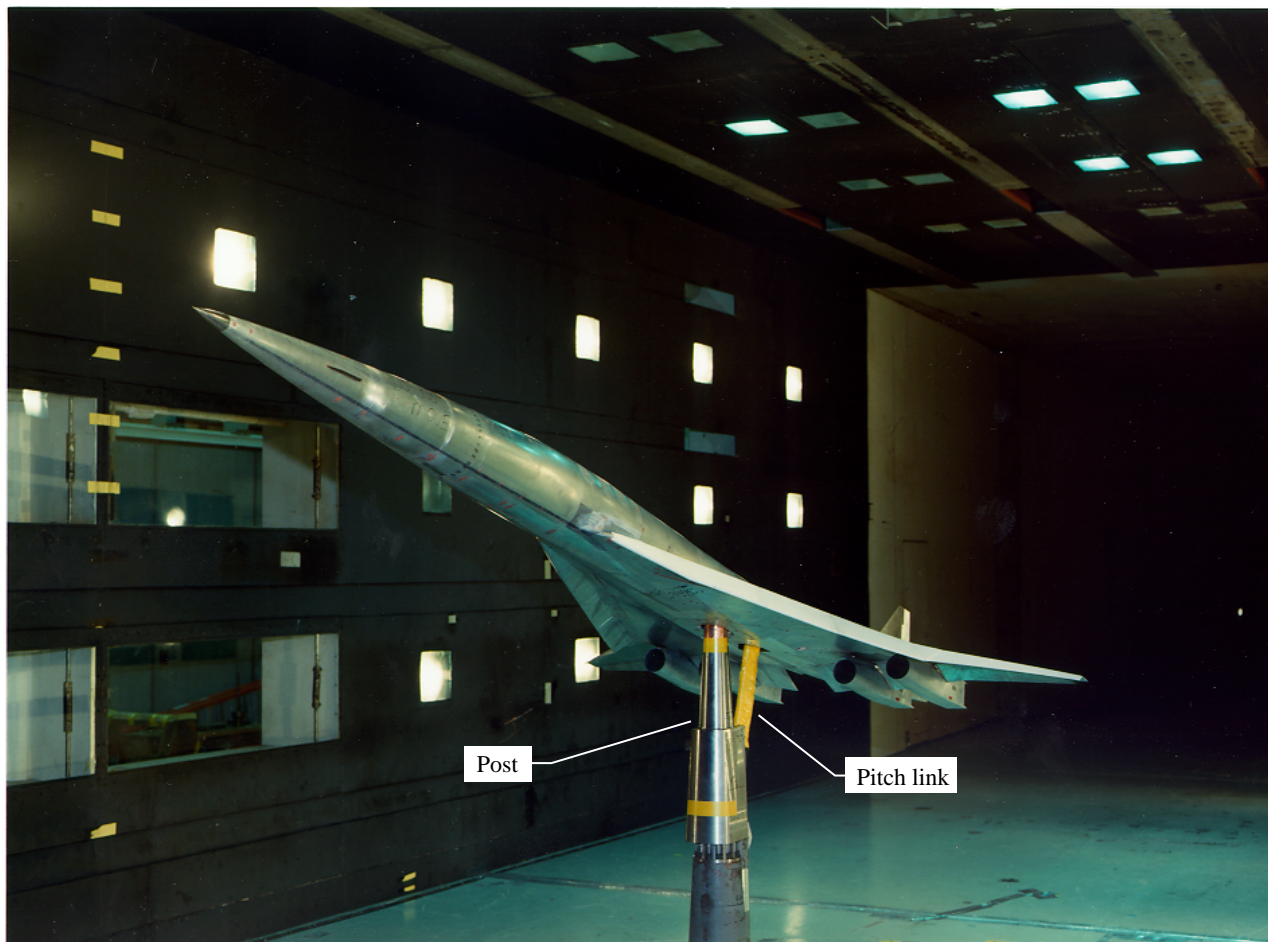


Figure 3. TCA model in Langley 14- by 22-Foot Subsonic Tunnel.

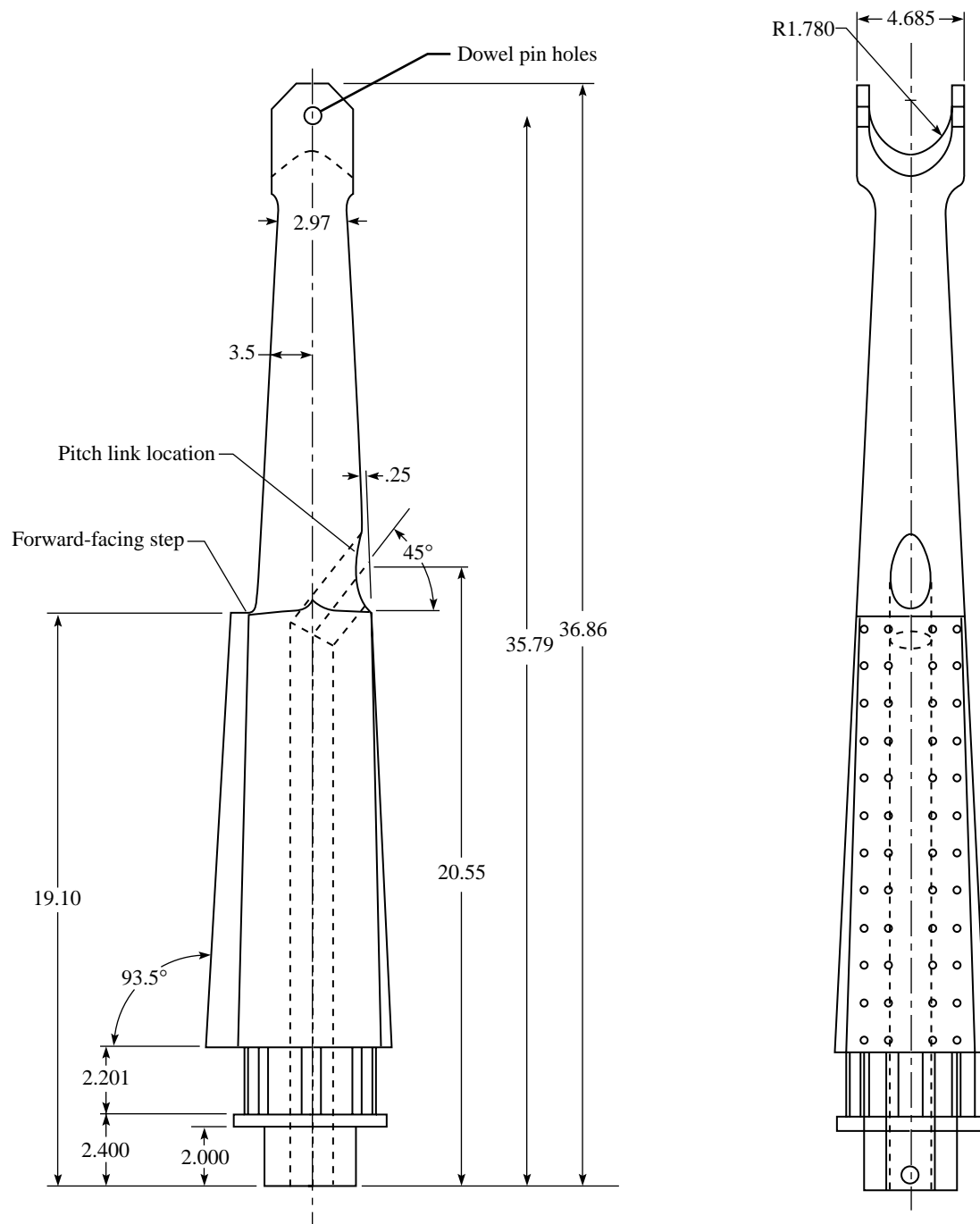


Figure 4. Drawing of model post. Linear dimensions are in inches.

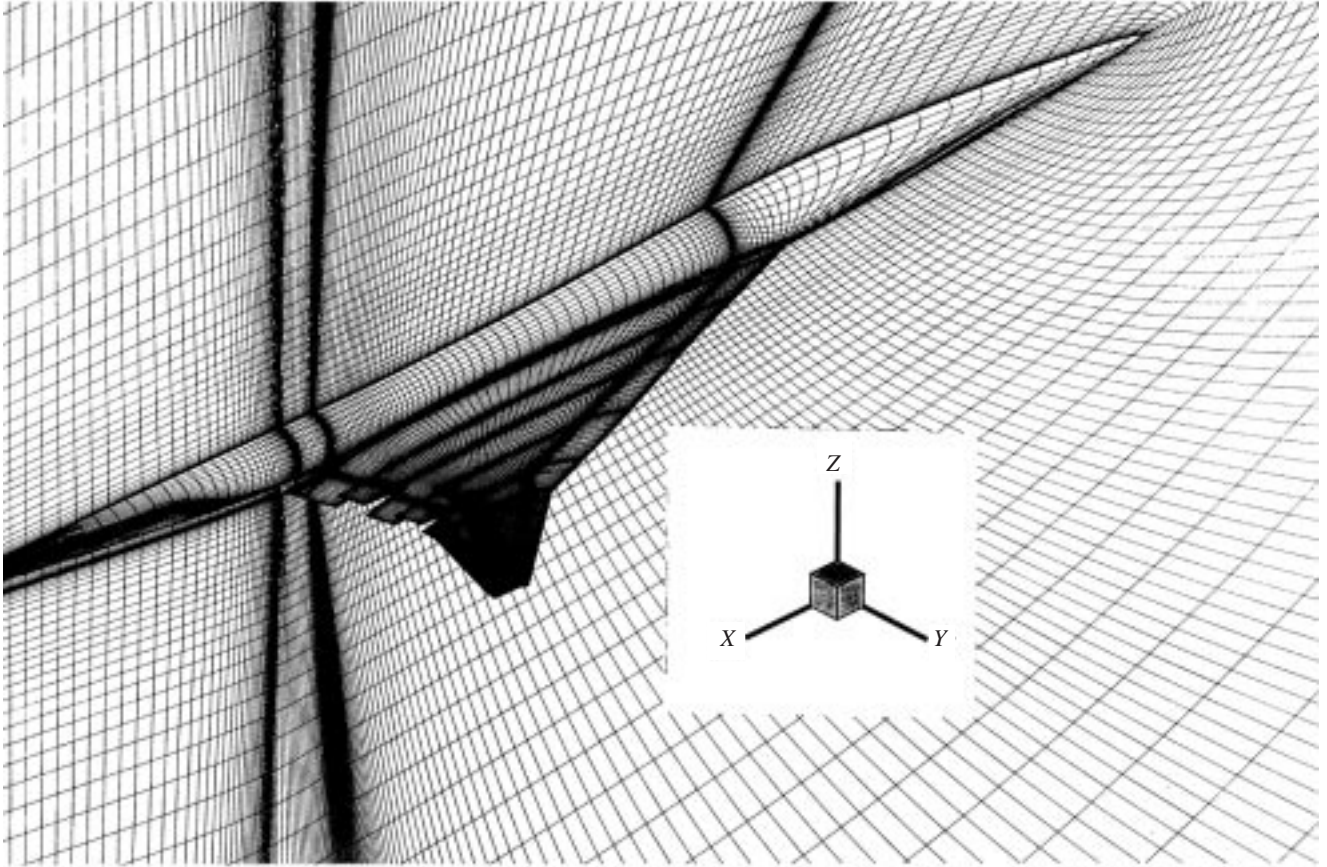


Figure 5. Surface grid of high-lift free-air TCA model plotted in symmetry plane.

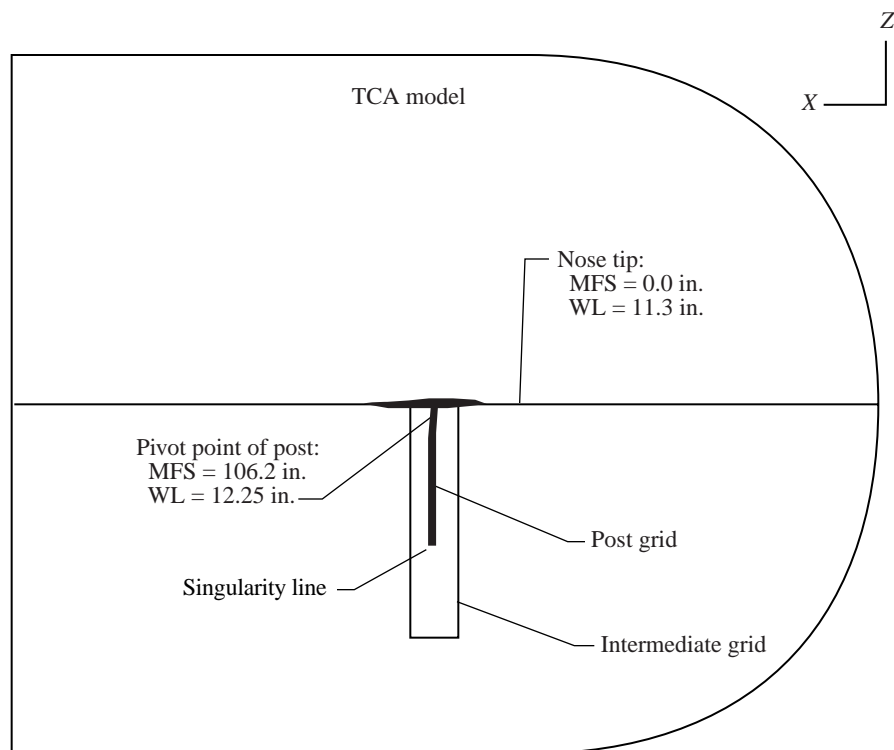


Figure 6. Outline of far-field boundary, post, and intermediate block.

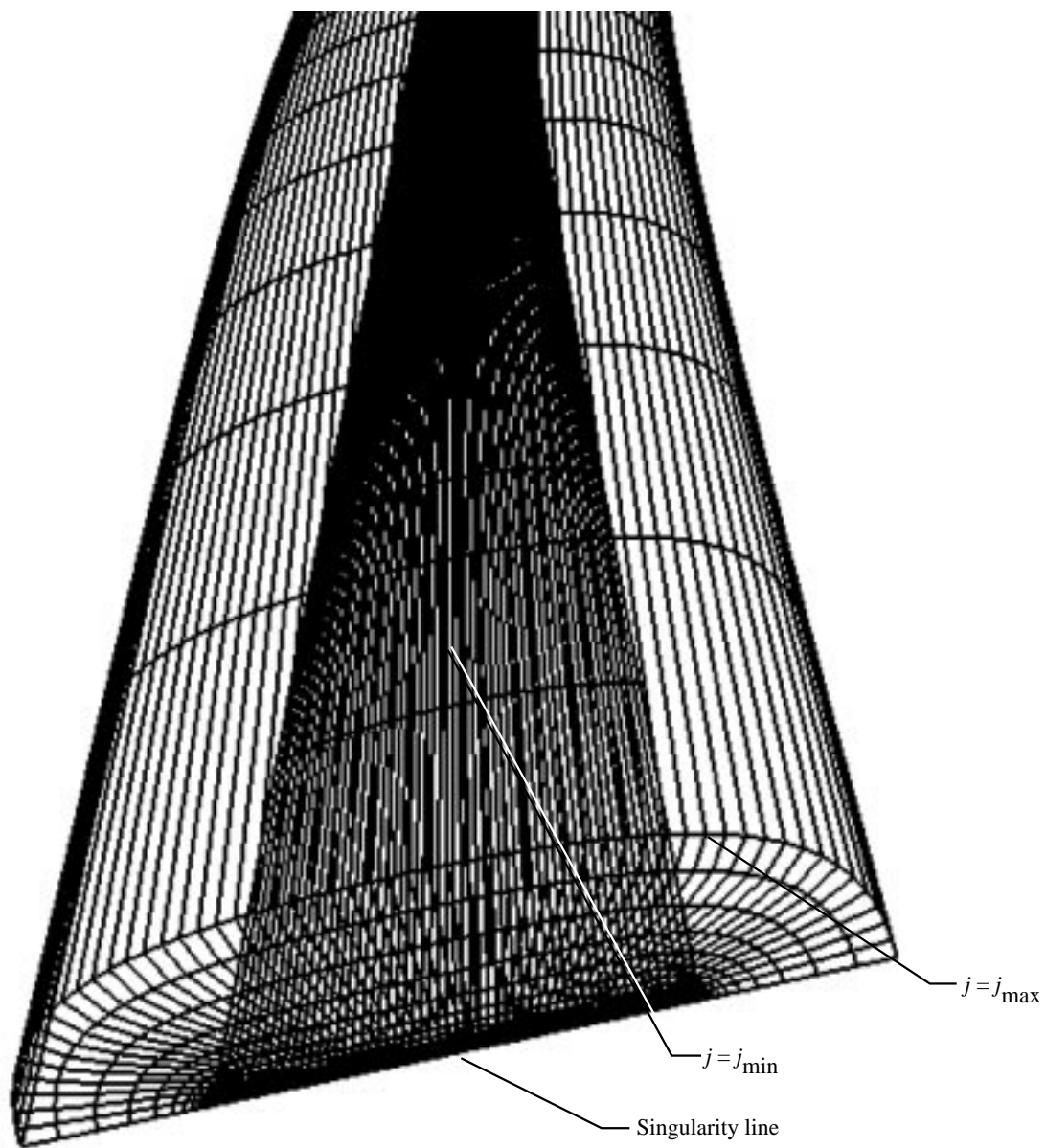


Figure 7. Close-up view of post grid, which shows end of post as singular line at $j = \min$.

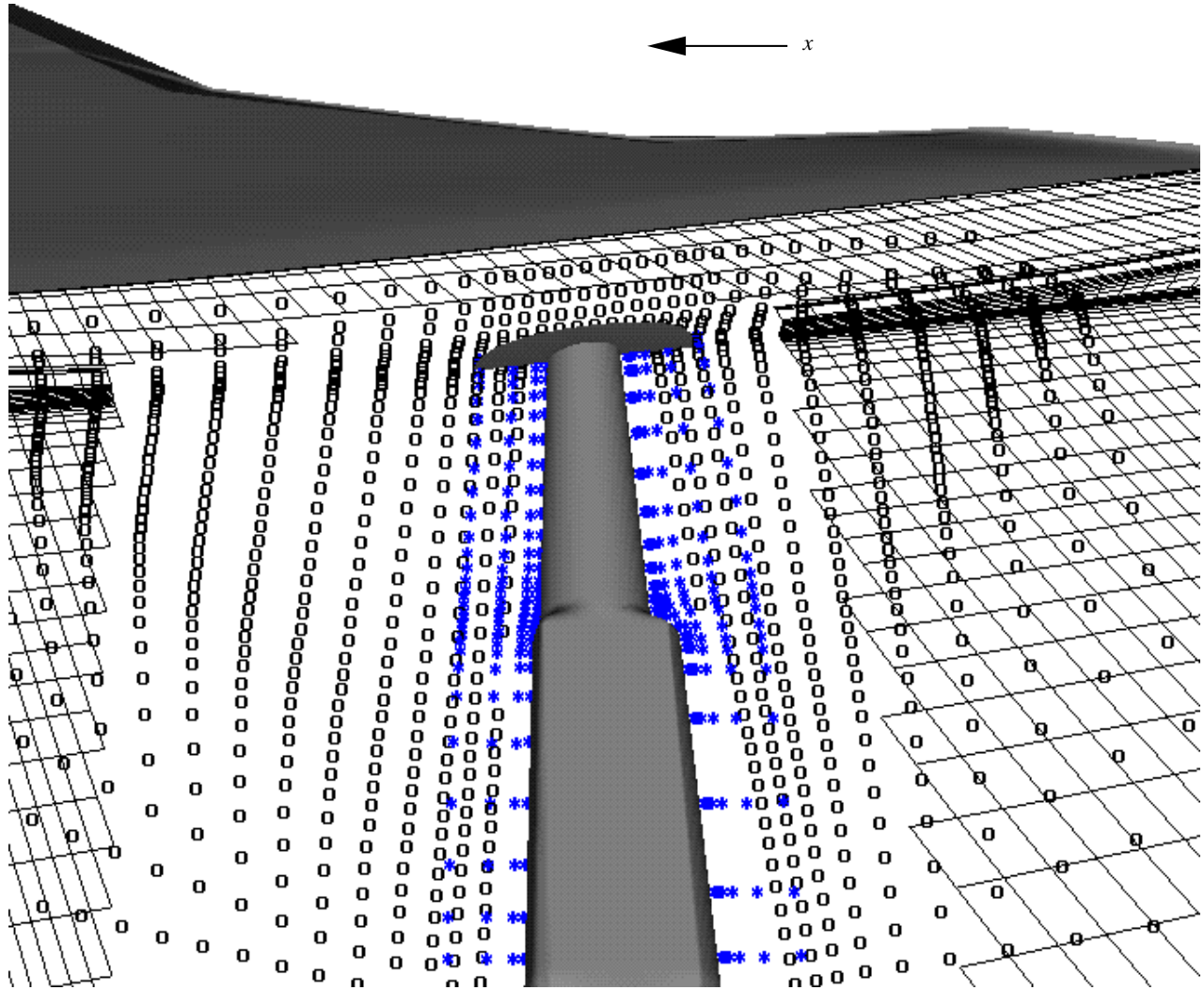


Figure 8. View of grid, which shows post mounted to bottom of TCA fuselage and other overset grids.

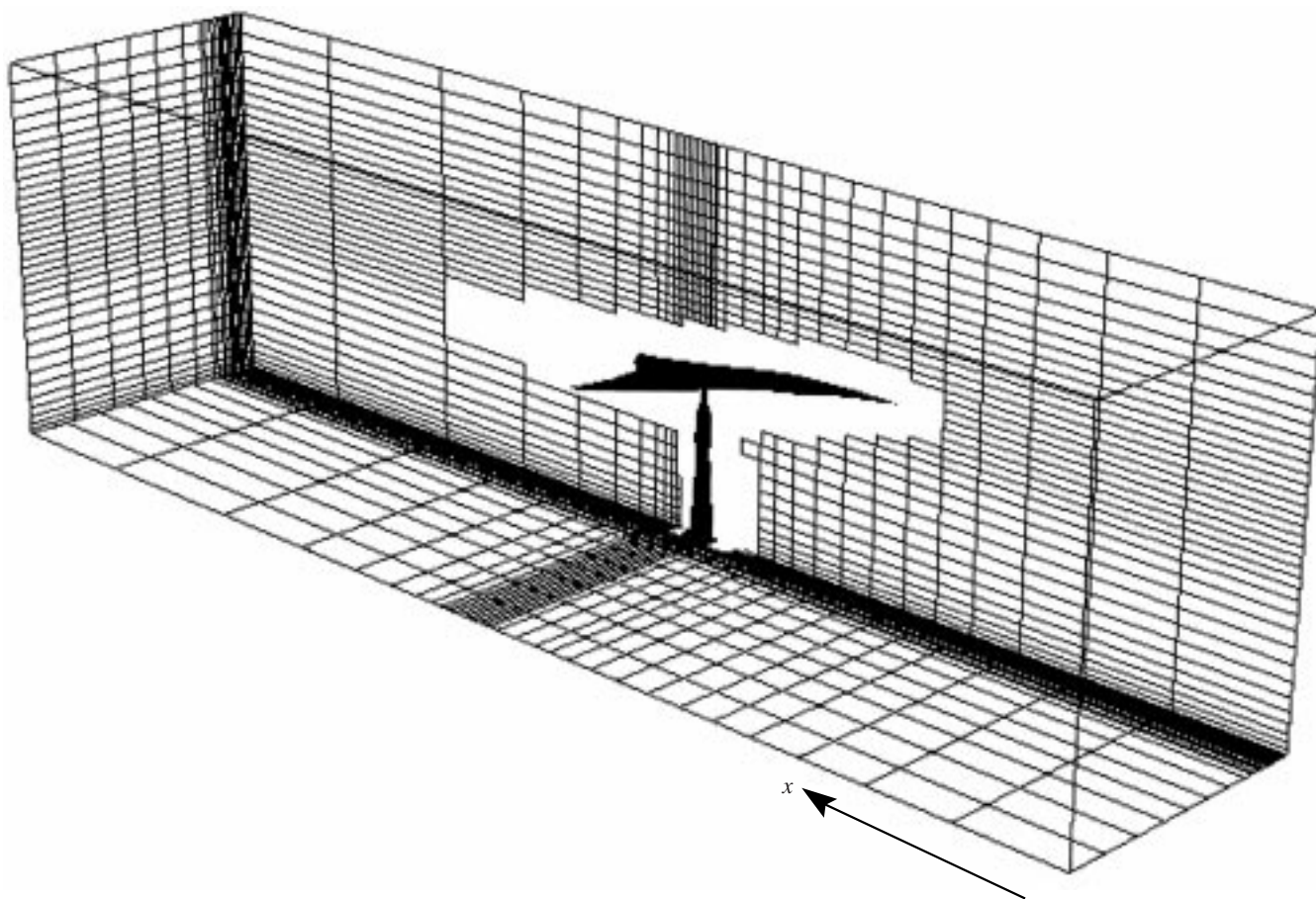


Figure 9. TCA surface grid and post grid shown inside Langley 14- by 22-Foot Subsonic Tunnel. Blanked-out area around model and post depict overset regions.

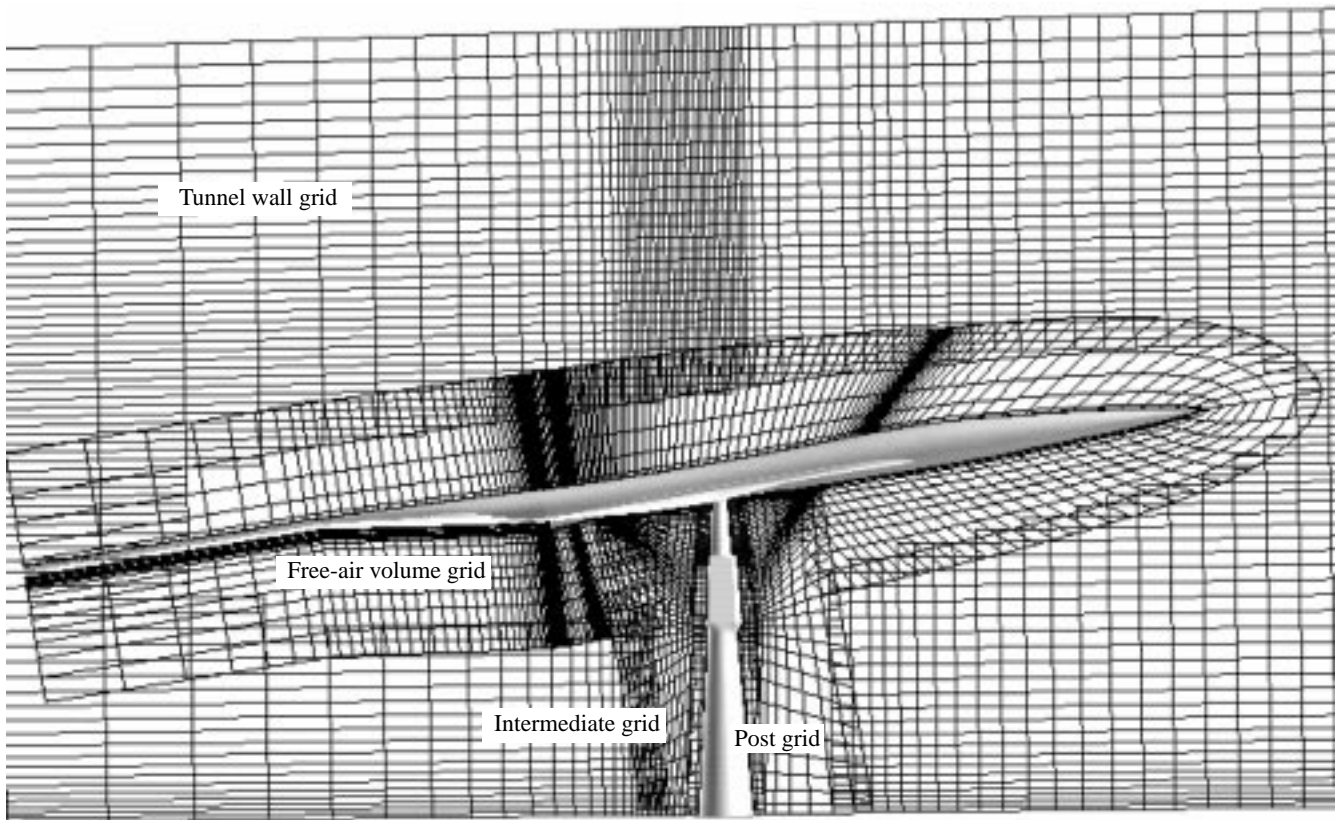


Figure 10. Grid of high-lift TCA shown post mounted in Langley 14- and 22-Foot Subsonic Tunnel.

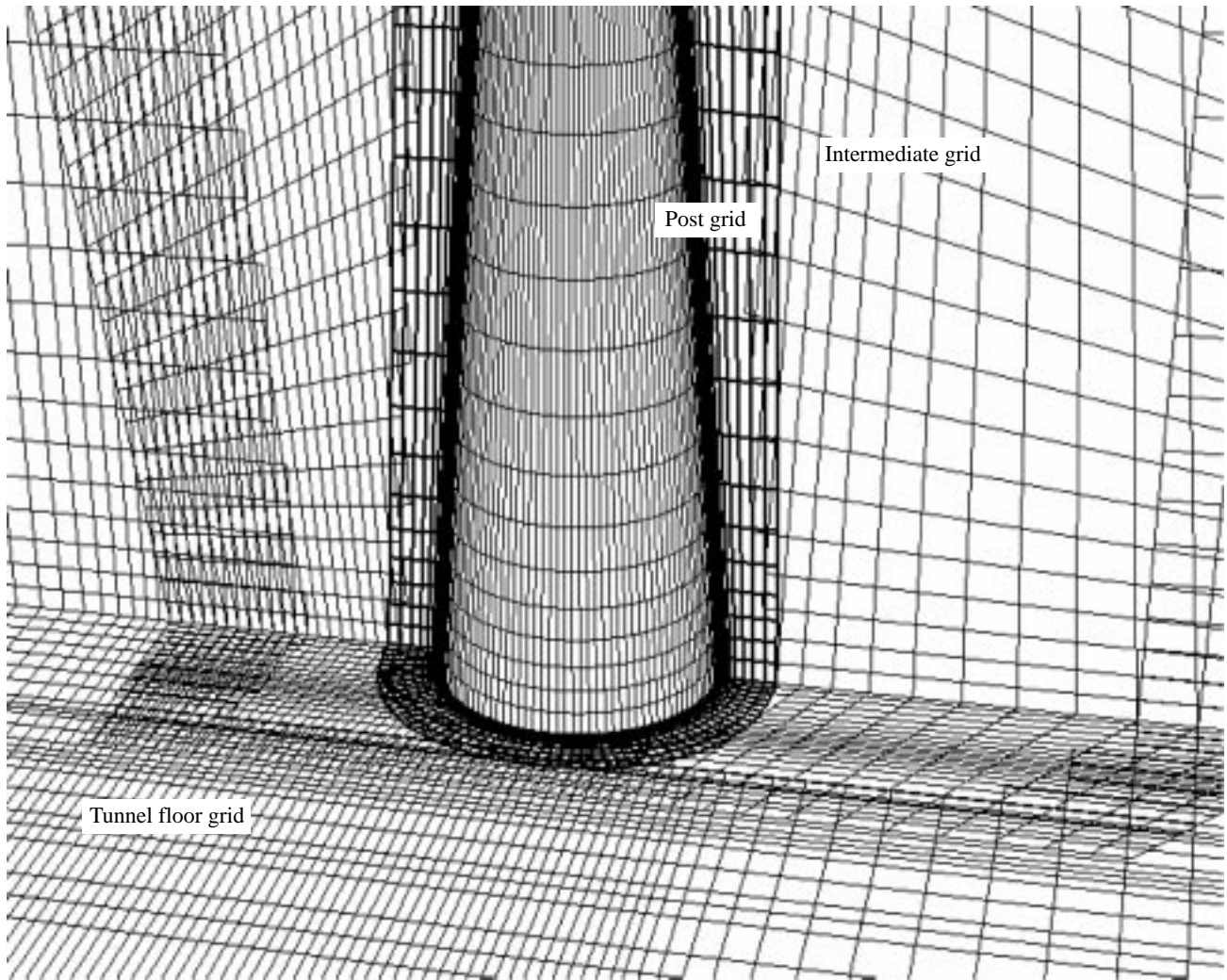


Figure 11. Post and intermediate grid overset onto wind-tunnel floor.

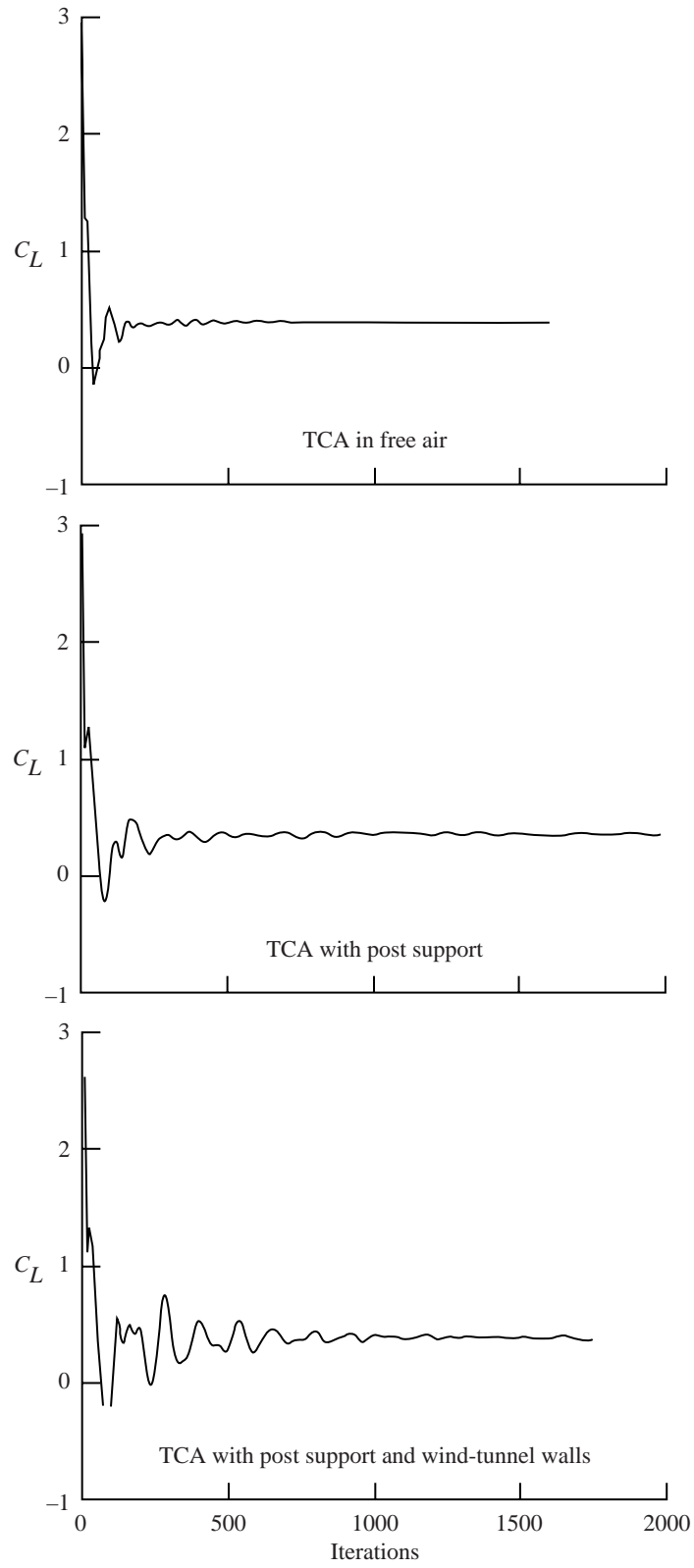
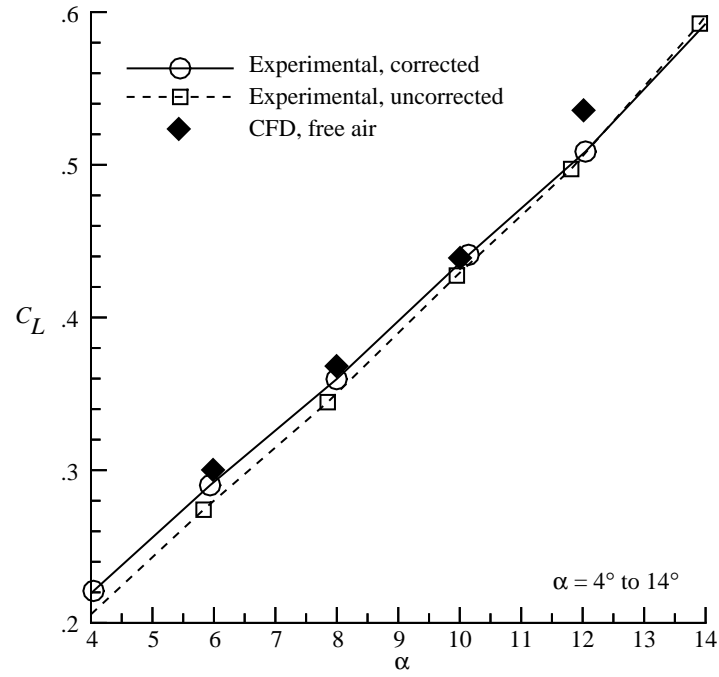
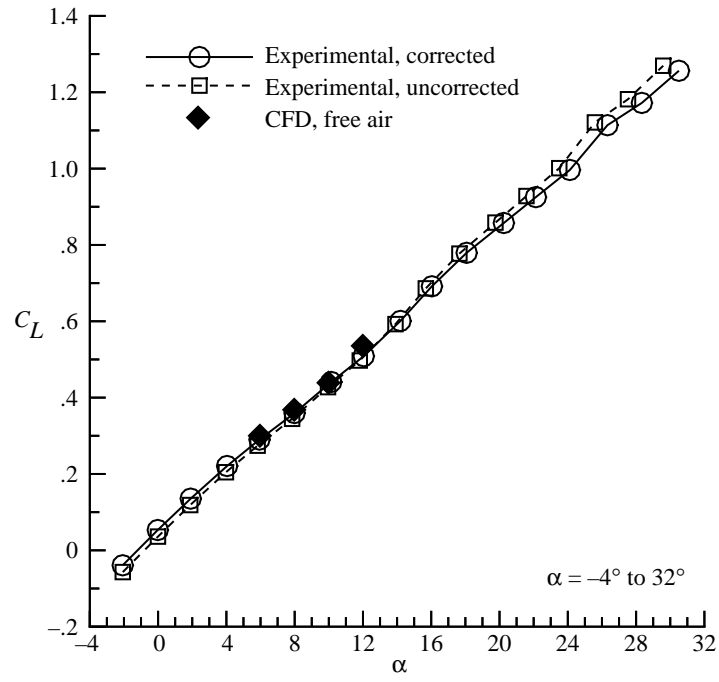
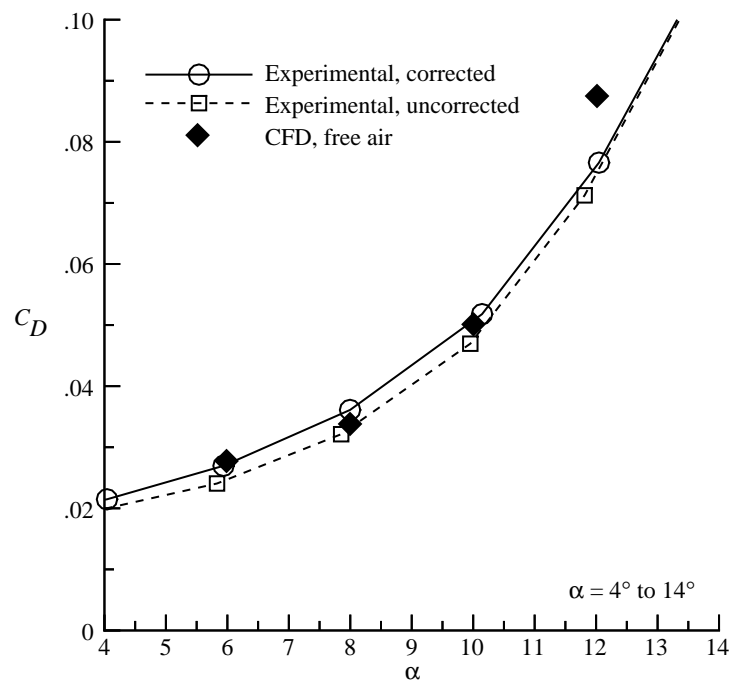
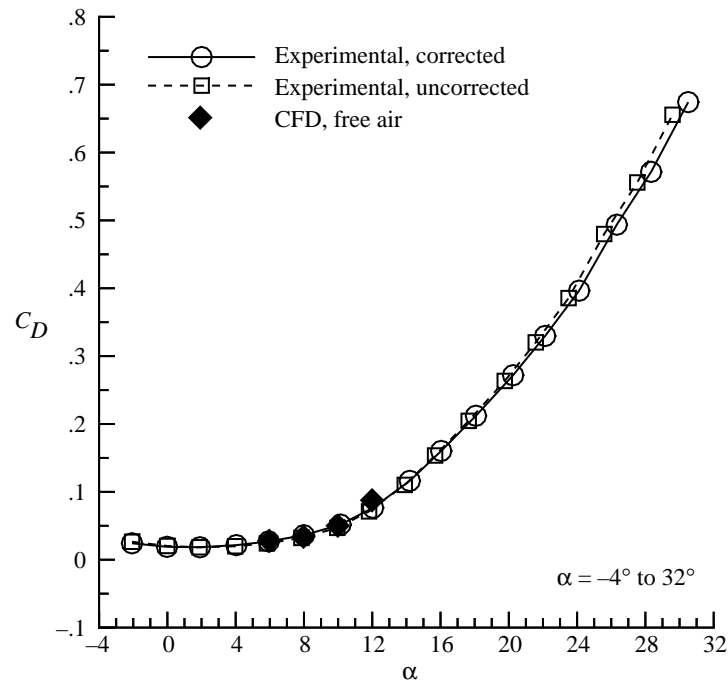


Figure 12. Lift coefficient convergence histories for three cases at $\alpha = 8^\circ$.



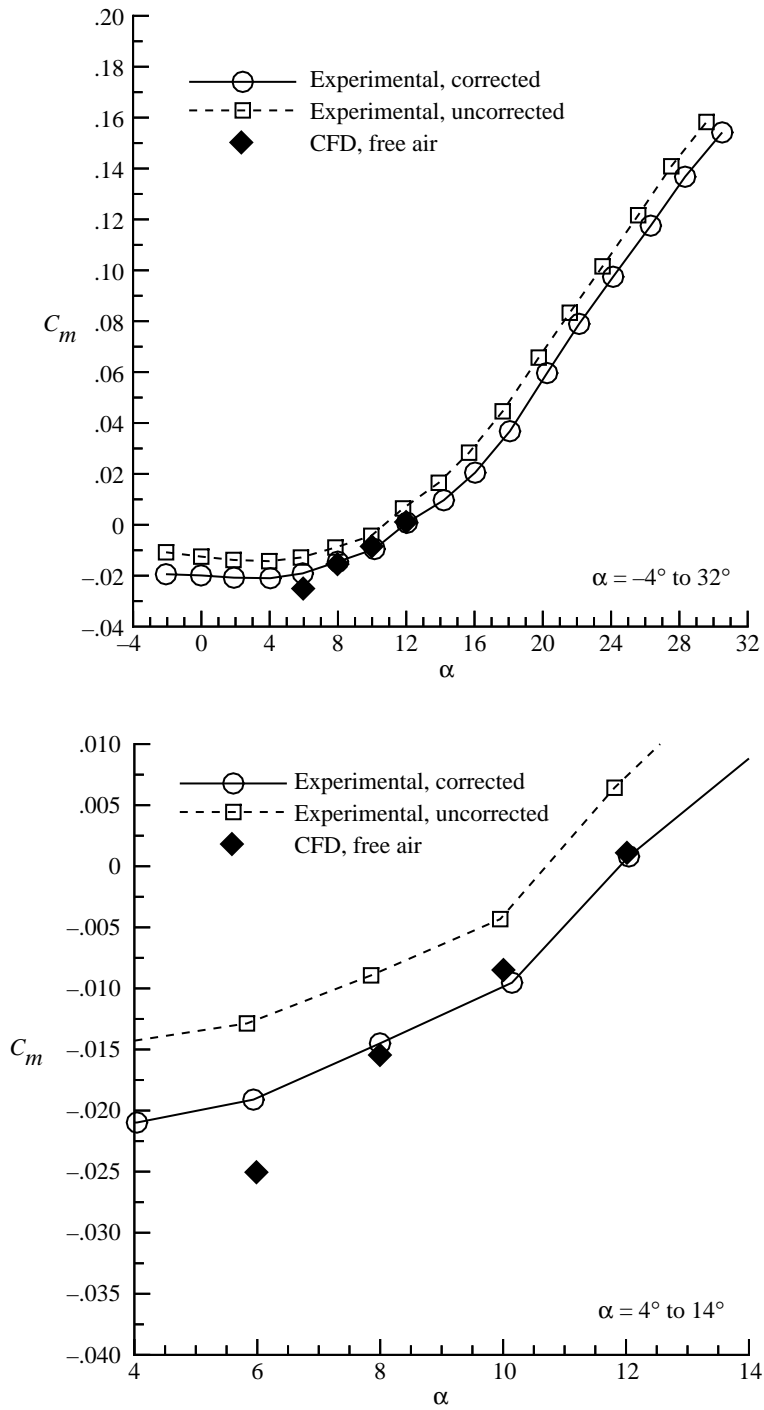
(a) Lift coefficient.

Figure 13. Experimental and computational data of TCA configuration at $M_\infty = 0.24$ and $Re_L = 1.4 \times 10^5$ per inch.



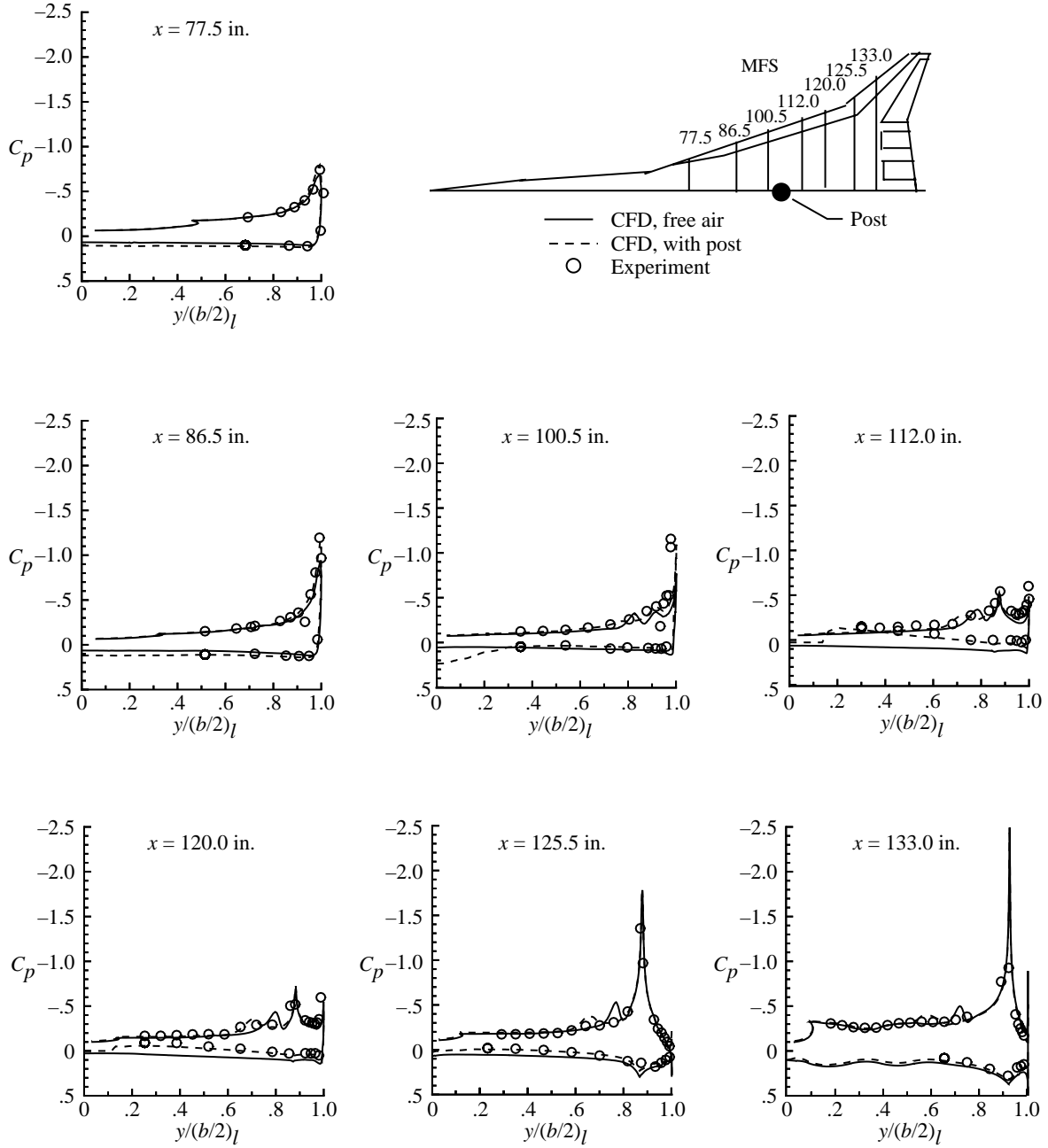
(b) Drag coefficient.

Figure 13. Continued.



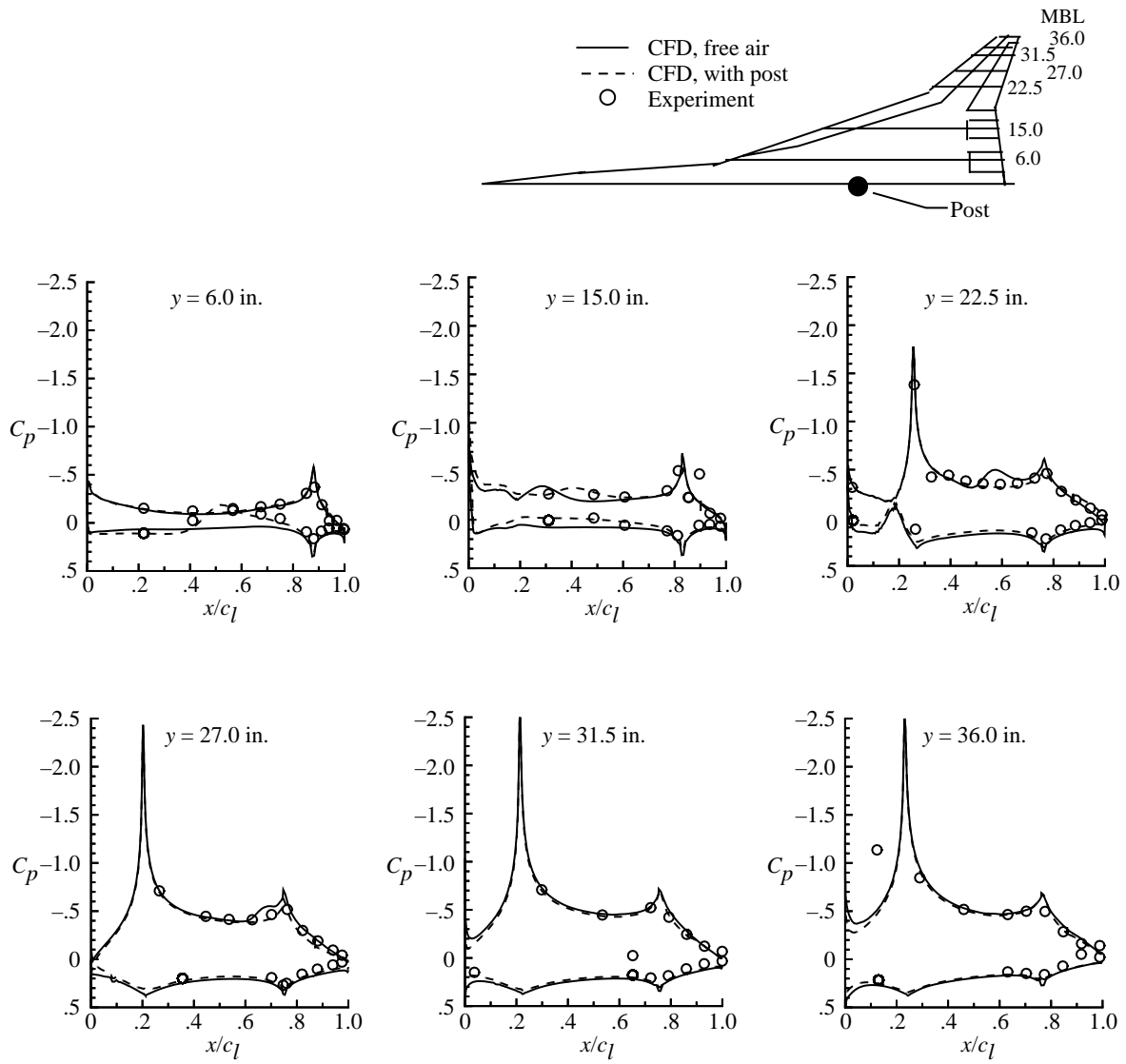
(c) Pitching moment.

Figure 13. Concluded.



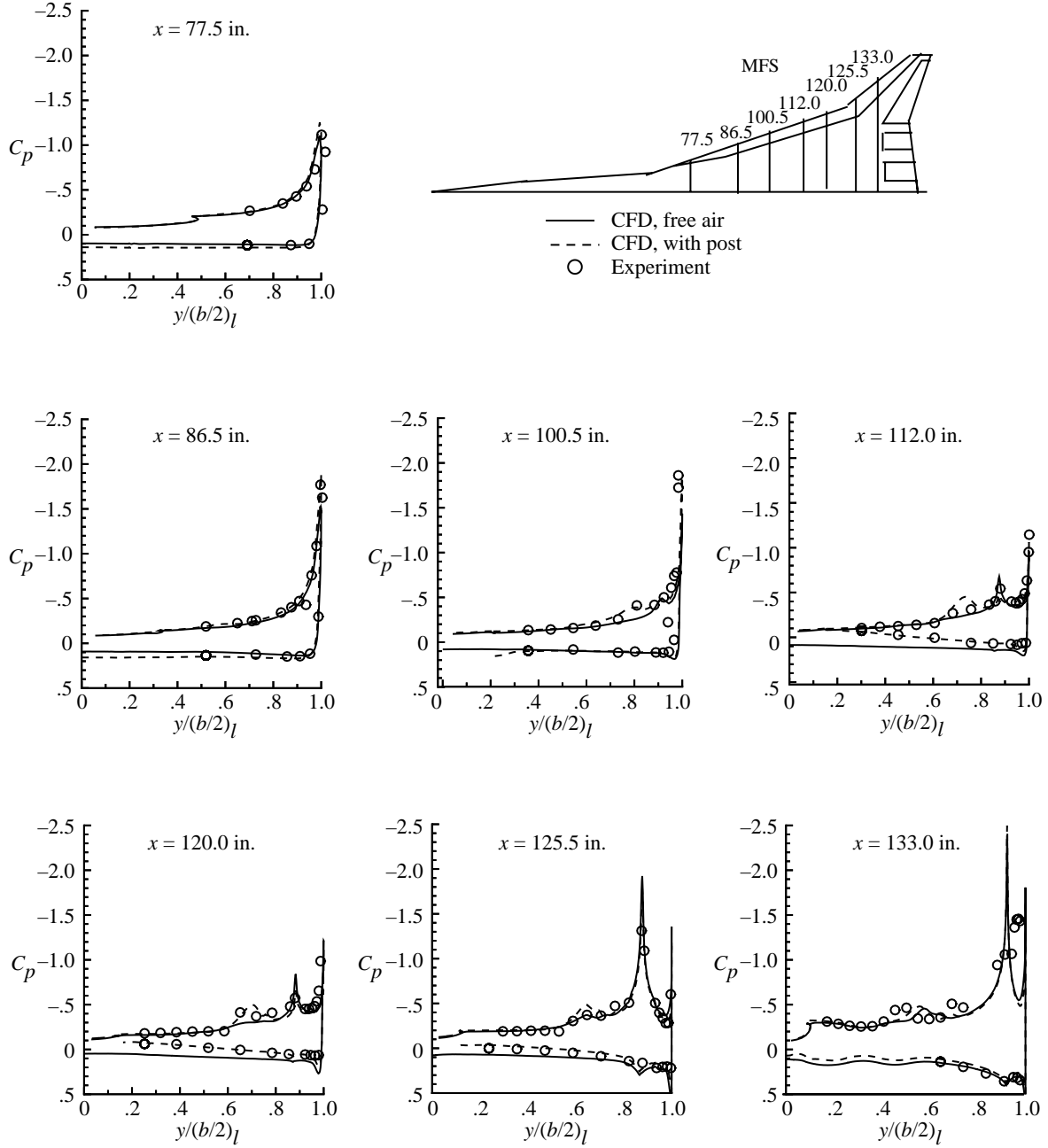
(a) Spanwise stations.

Figure 14. Experimental and computational results for TCA configuration at $\alpha = 6^\circ$, $M_\infty = 0.24$, and $Re_L = 1.4 \times 10^5$ per inch.



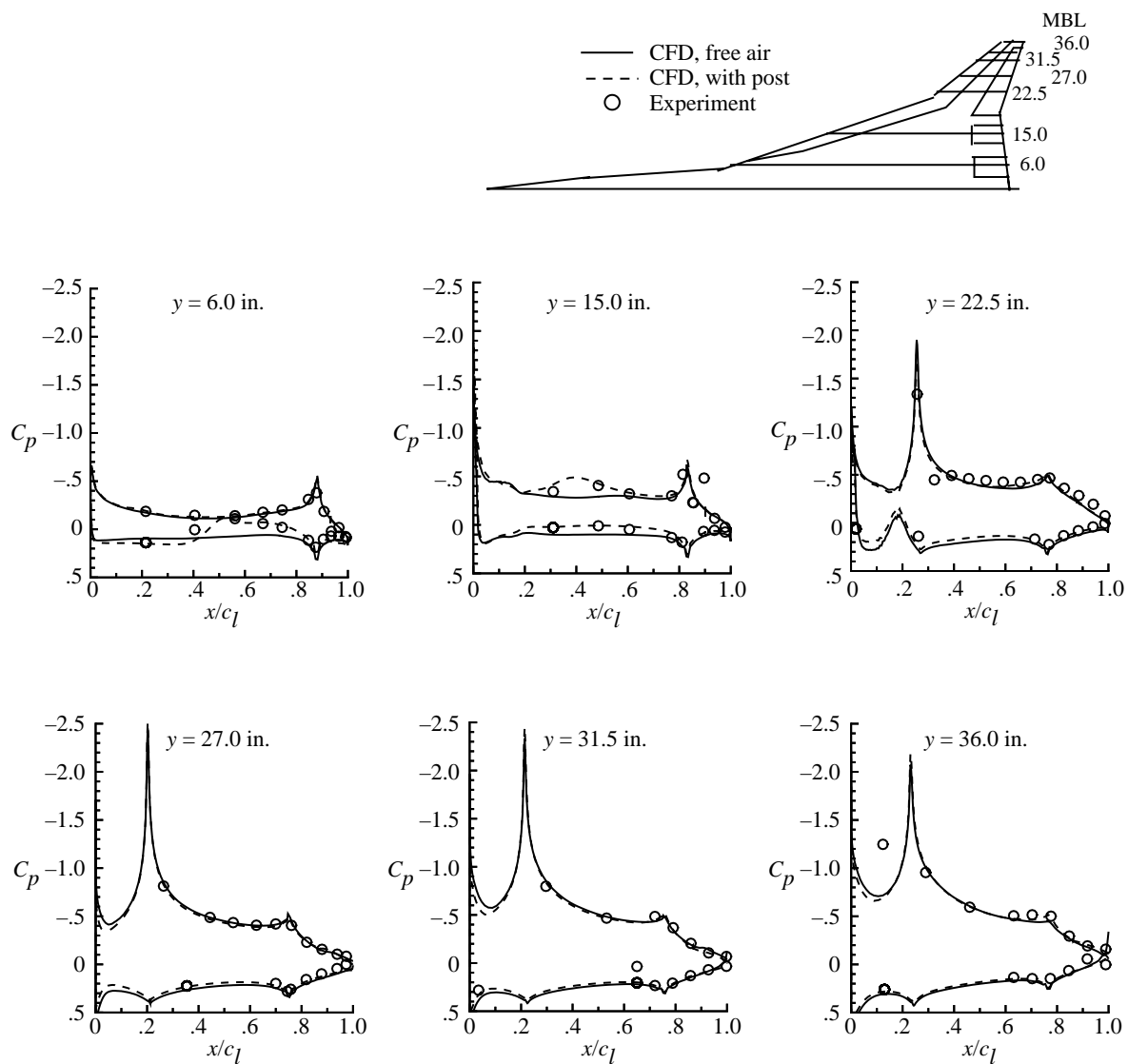
(b) Streamwise stations.

Figure 14. Concluded.



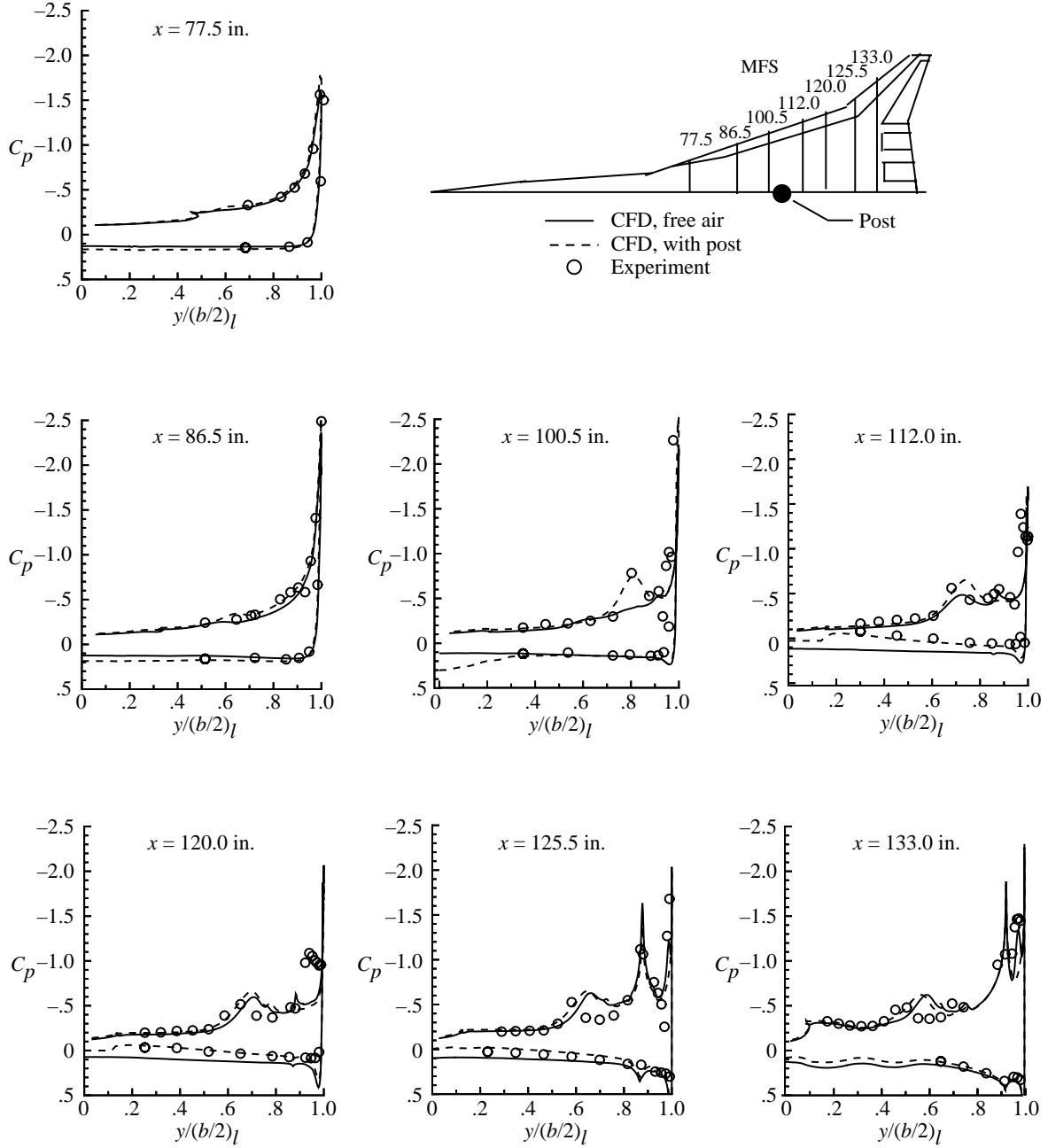
(a) Spanwise stations.

Figure 15. Experimental and computational results for TCA configuration at $\alpha = 8^\circ$, $M_\infty = 0.24$, and $Re_L = 1.4 \times 10^5$ per inch.



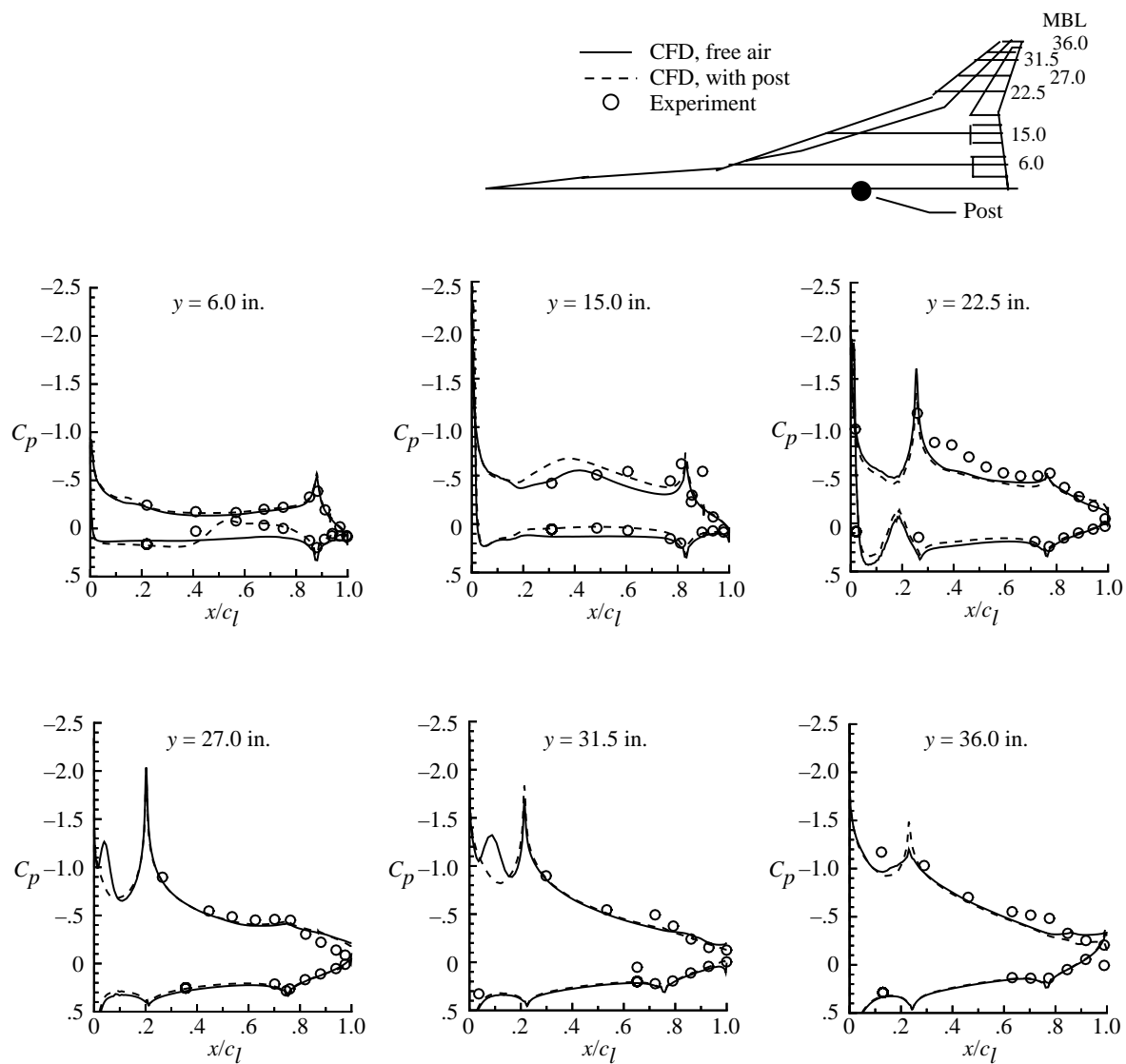
(b) Streamwise stations.

Figure 15. Concluded.



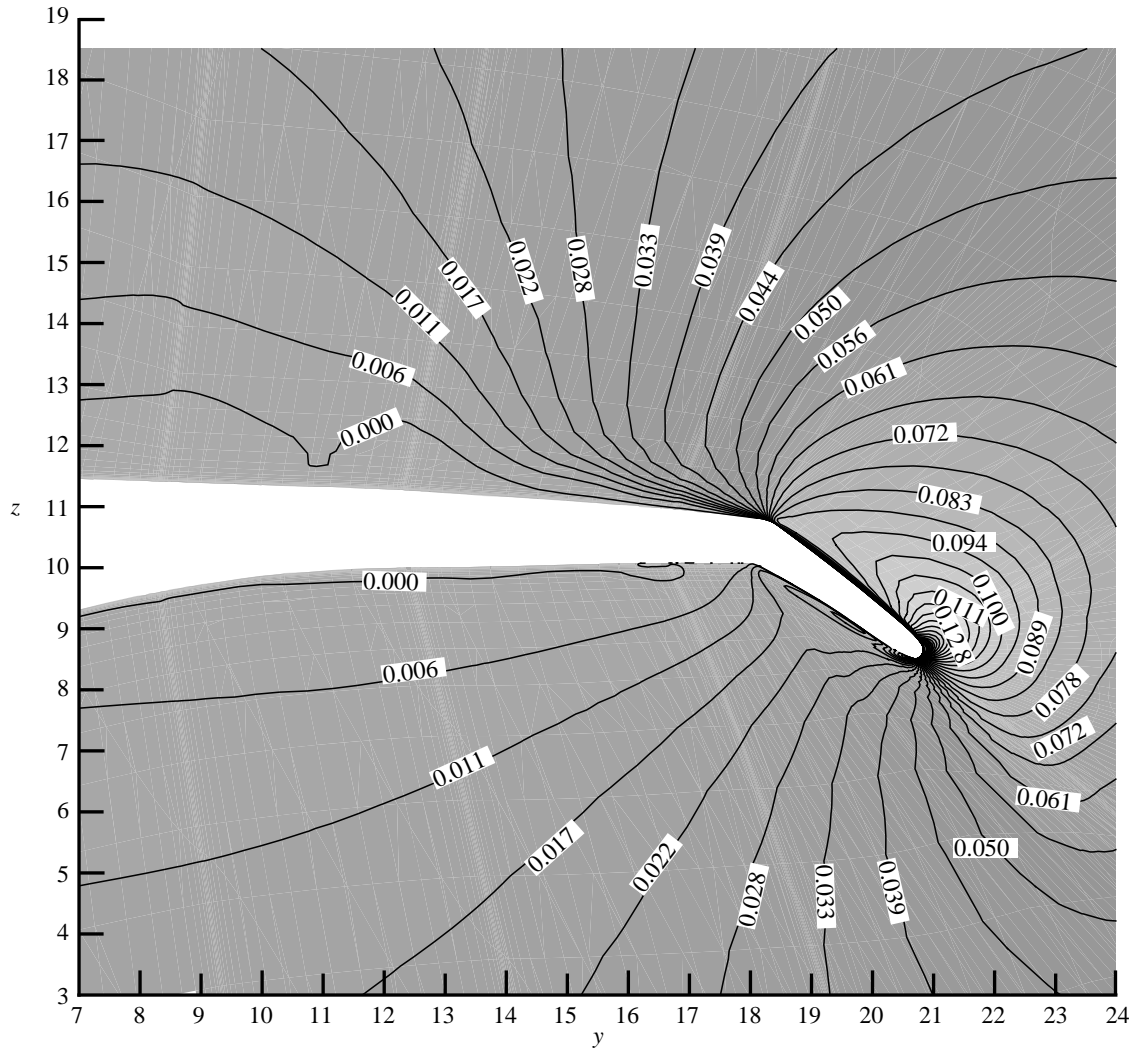
(a) Spanwise stations.

Figure 16. Experimental and computational results for TCA configuration at $\alpha = 10^\circ$, $M_\infty = 0.24$, and $Re_L = 1.4 \times 10^5$ per inch.



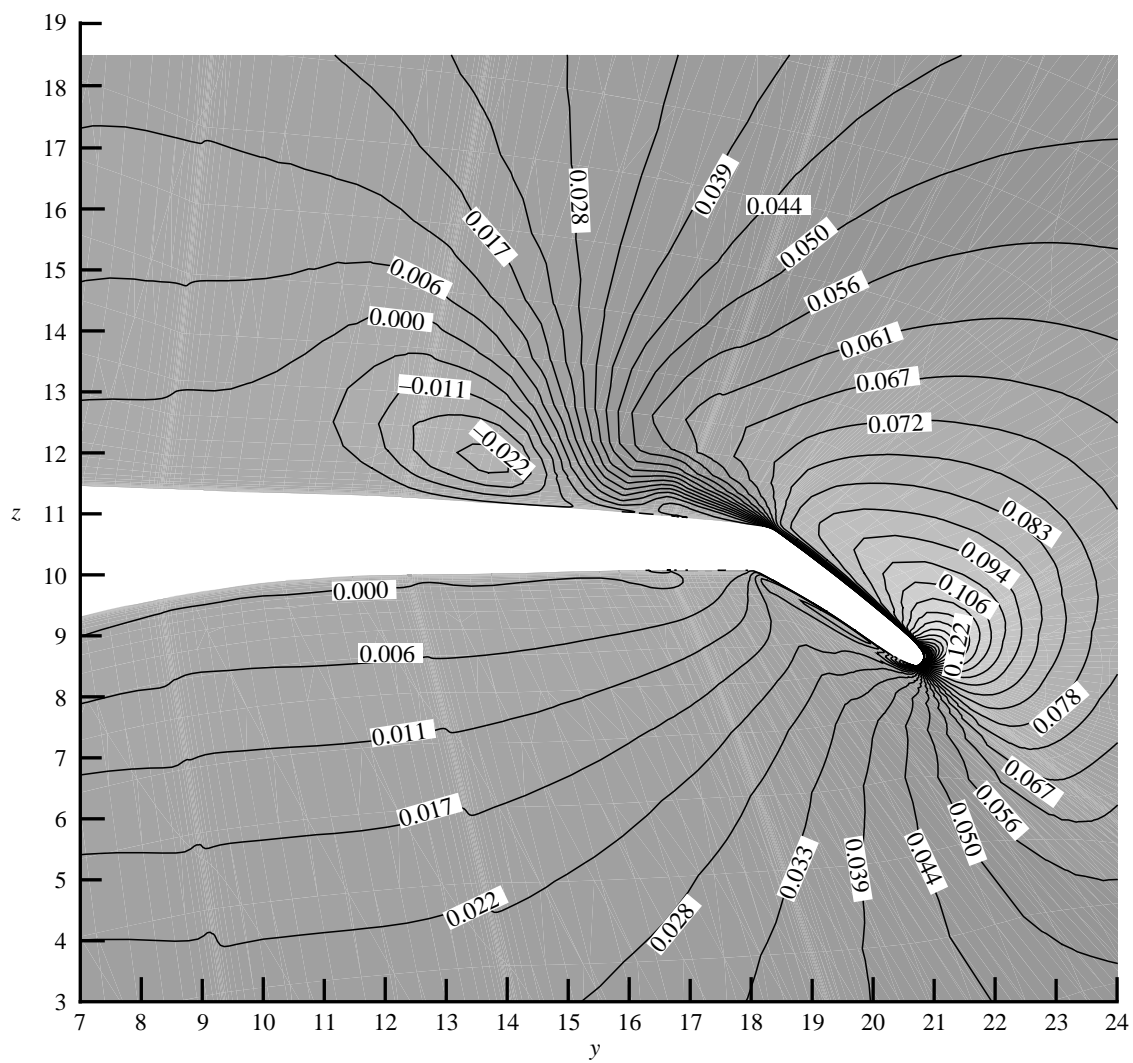
(b) Streamwise stations.

Figure 16. Concluded.



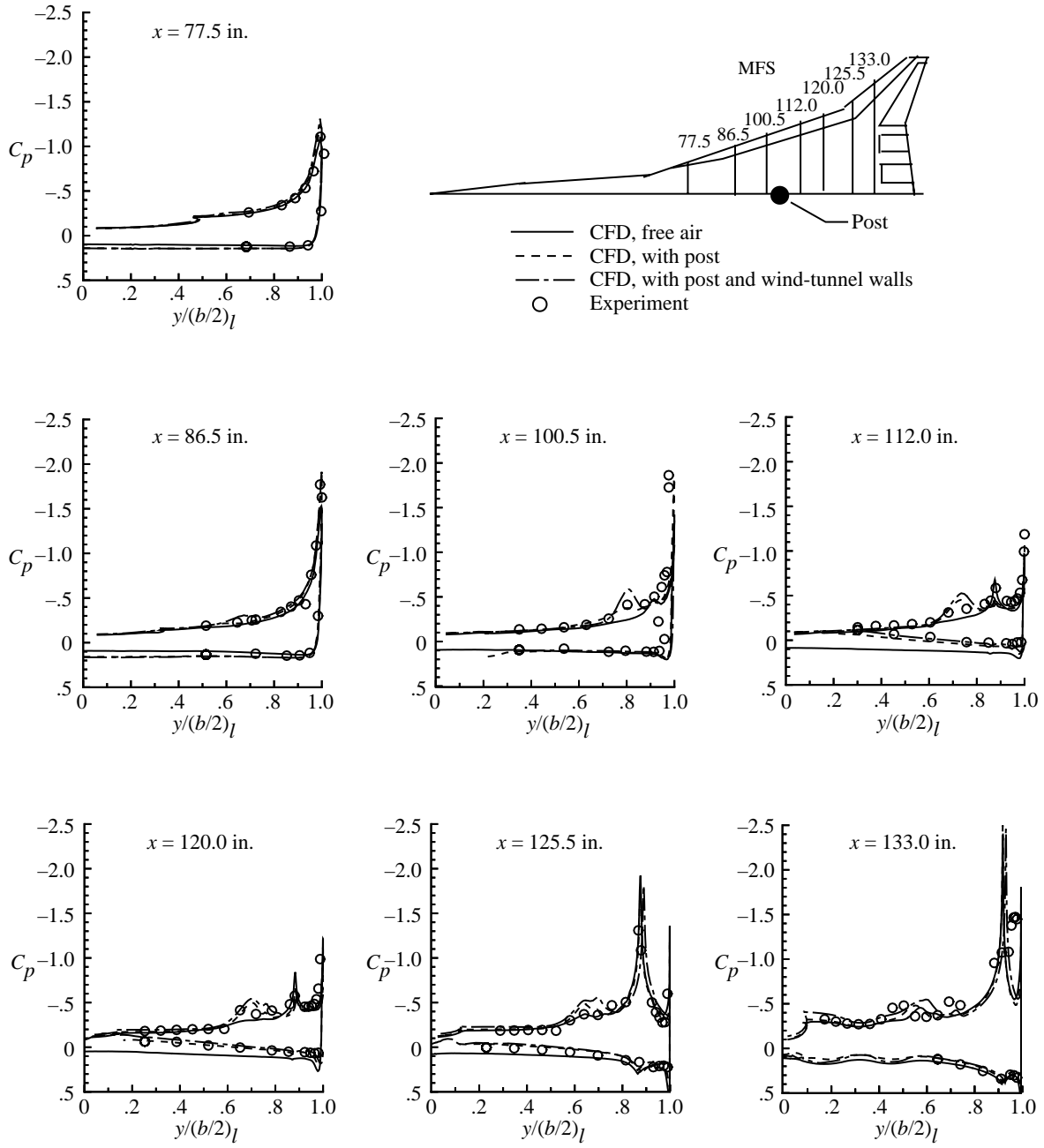
(a) Free air.

Figure 17. Contours of w -component of velocity extracted in cross-flow plane at $x = 115$ in., $\alpha = 8^\circ$, $M_\infty = 0.24$, and $Re_L = 1.4 \times 10^5$ per inch.



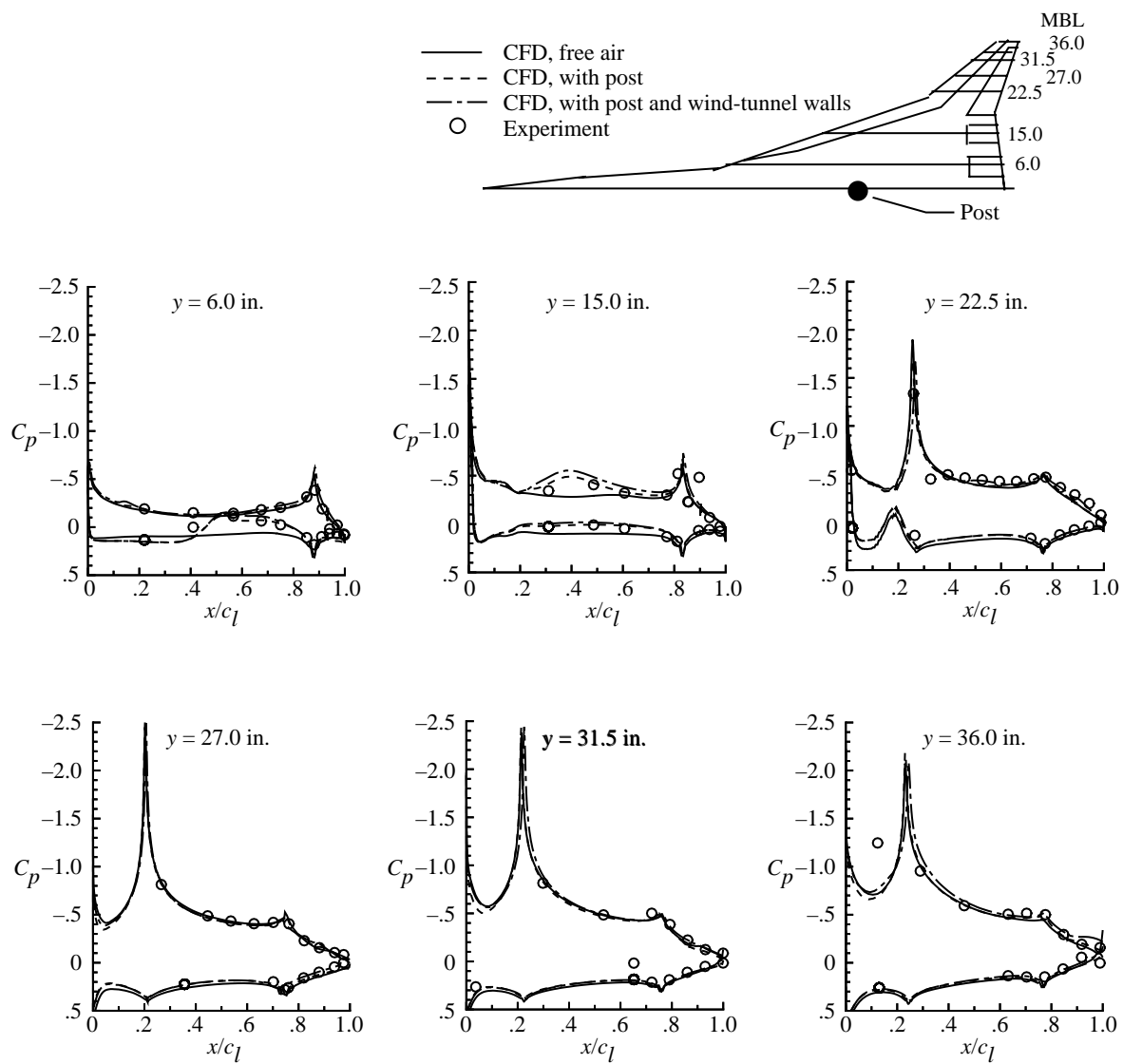
(b) Post support.

Figure 17. Concluded.



(a) Spanwise stations.

Figure 18. Experimental and computational results for all three cases for TCA configuration at $\alpha = 8^\circ$, $M_\infty = 0.24$, and $Re_L = 1.4 \times 10^5$ per inch.



(b) Streamwise stations.

Figure 18. Concluded.

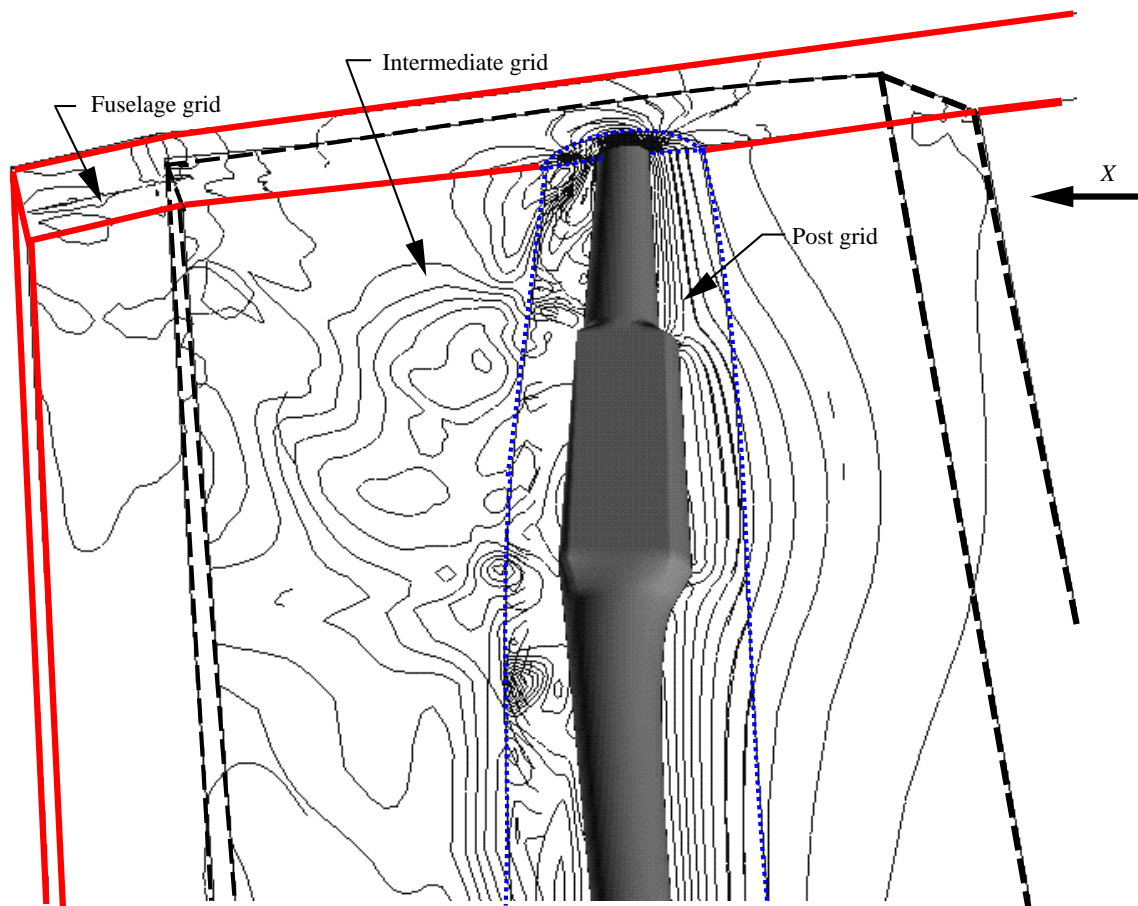


Figure 19. Overset region depicting continuity of pressure contour lines. Post and intermediate grid overset onto surrounding fuselage grid; $\alpha = 8^\circ$, $M_\infty = 0.24$, and $Re_L = 1.4 \times 10^5$ per inch.

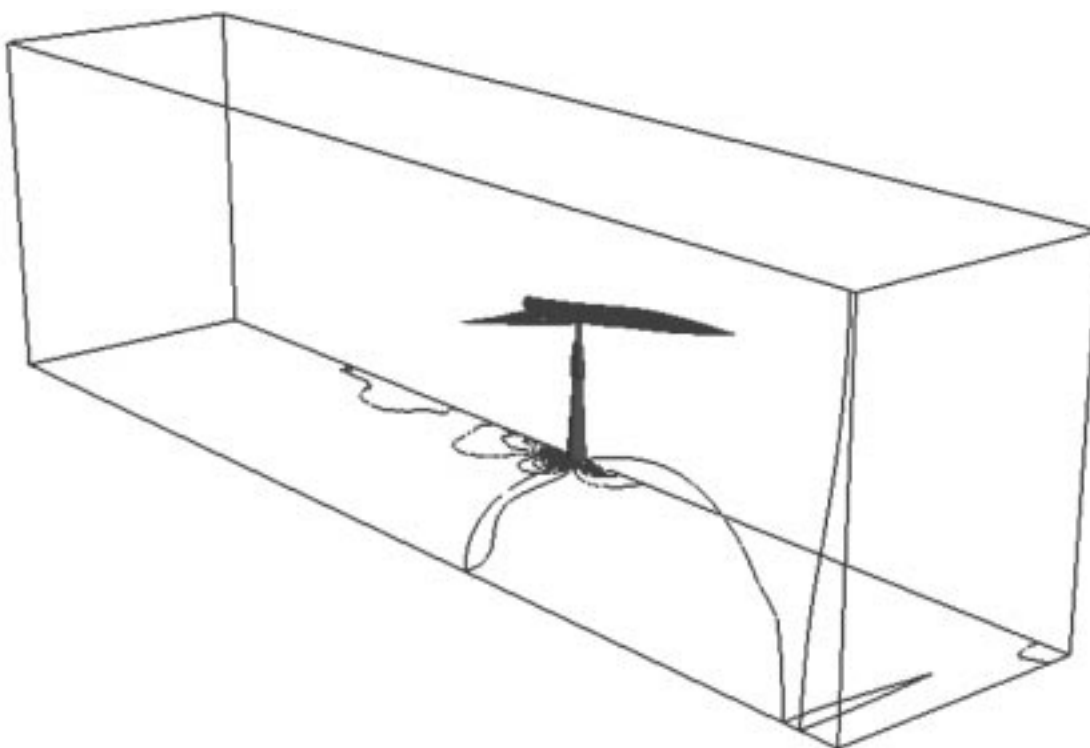
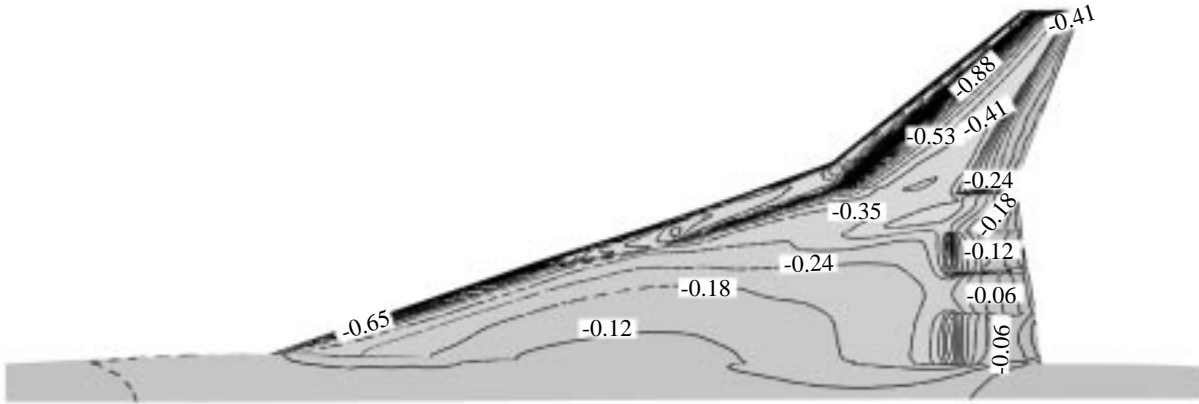
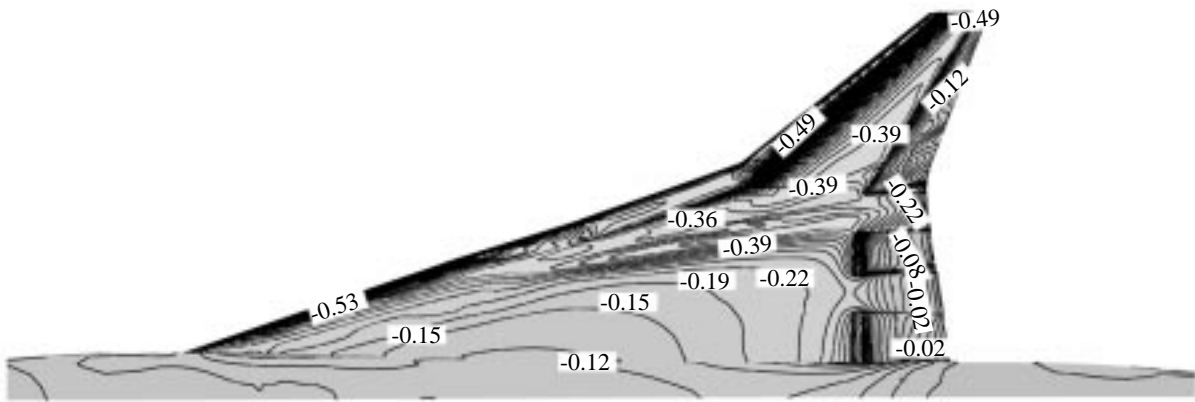


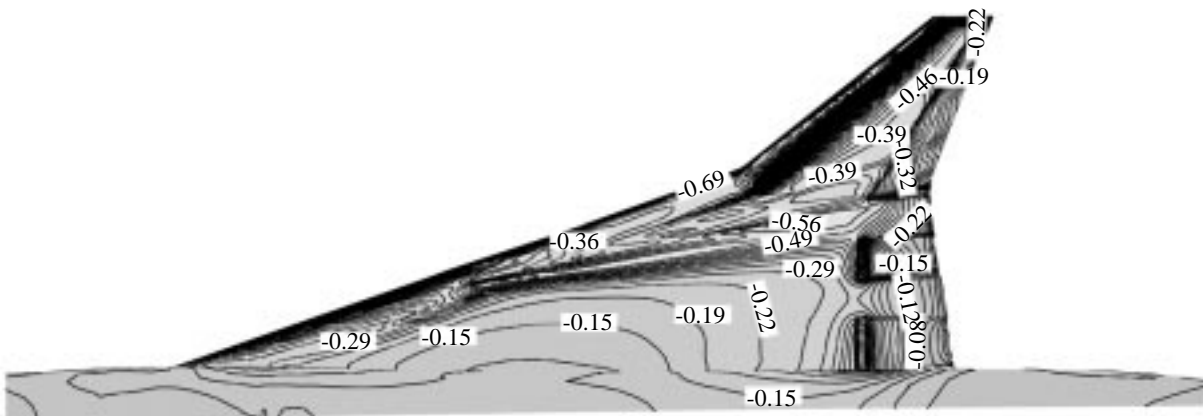
Figure 20. Pressure contours on Langley 14- by 22-Foot Subsonic Tunnel walls at $\alpha = 8^\circ$, $M_\infty = 0.24$, and $\text{Re}_L = 1.4 \times 10^5$ per inch.



(a) Free air.

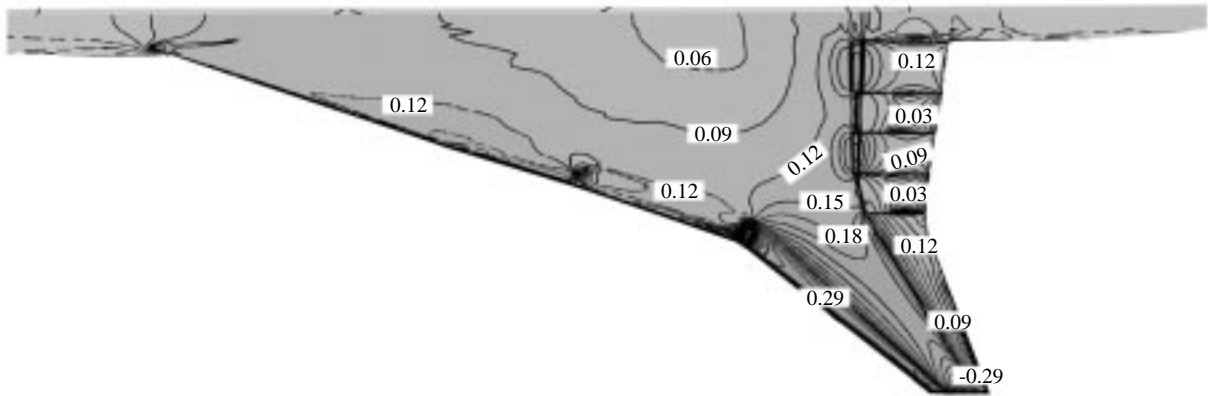


(b) Post support.

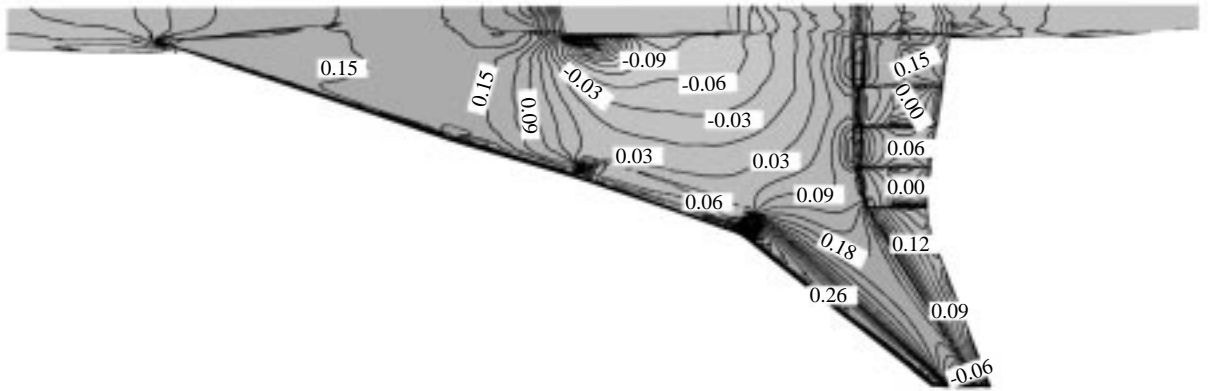


(c) Post support and wind-tunnel walls.

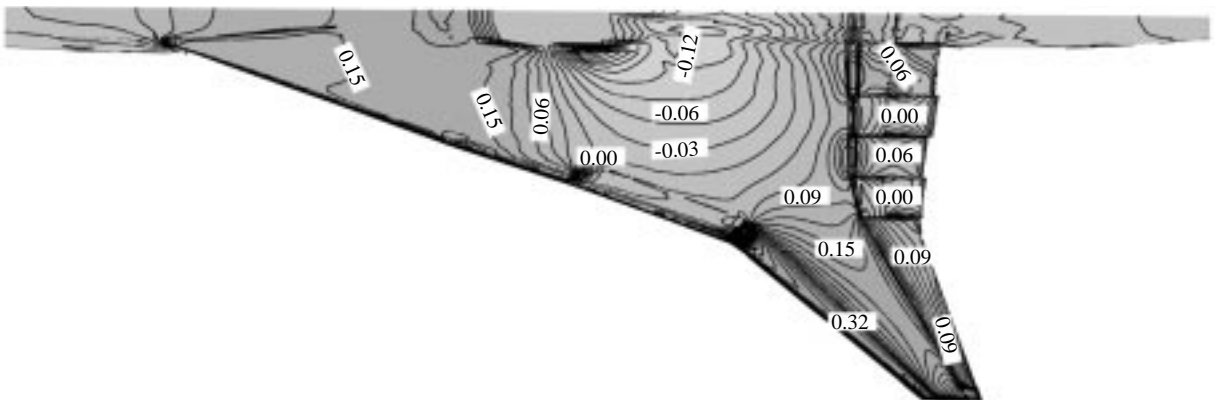
Figure 21. Upper surface pressure coefficients for TCA configuration at $\alpha = 8^\circ$, $M_\infty = 0.24$, and $Re_L = 1.4 \times 10^5$ per inch.



(a) Free air.

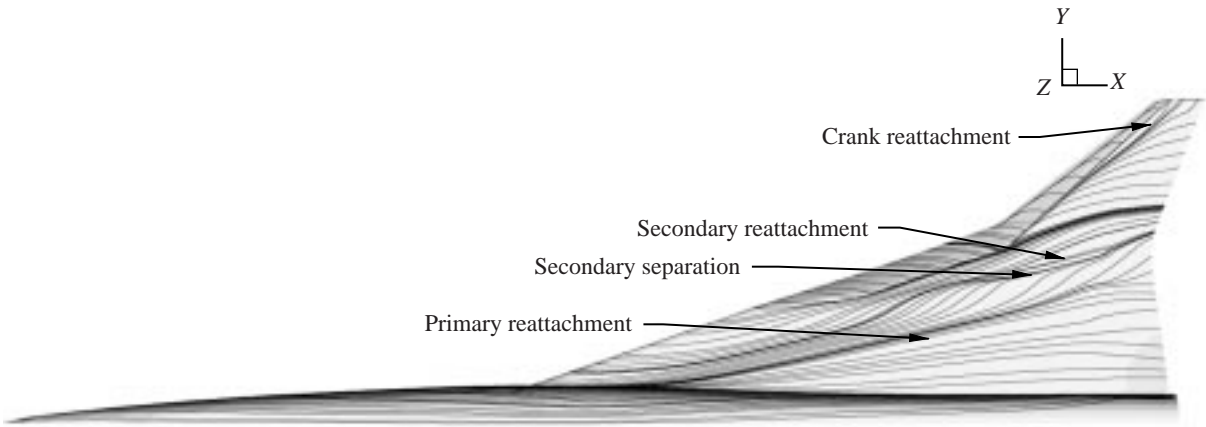


(b) Post support.

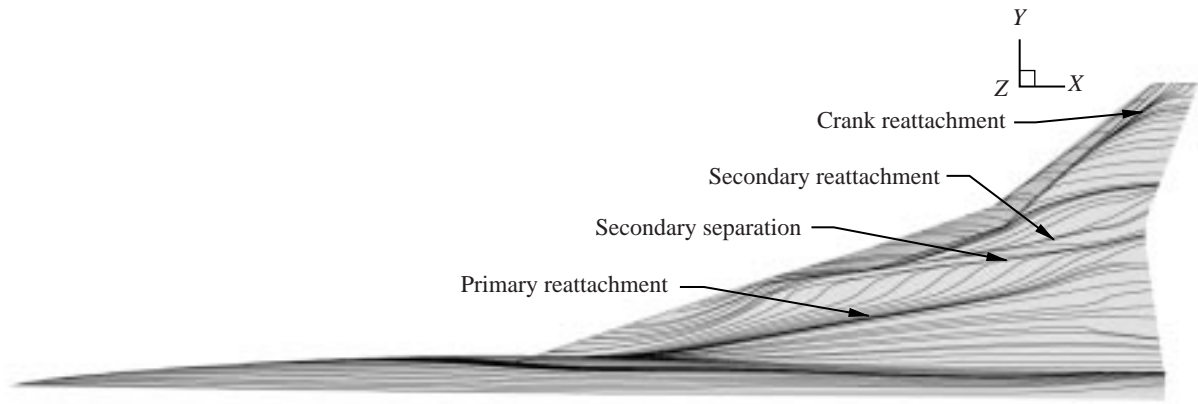


(c) Post support and wind-tunnel walls.

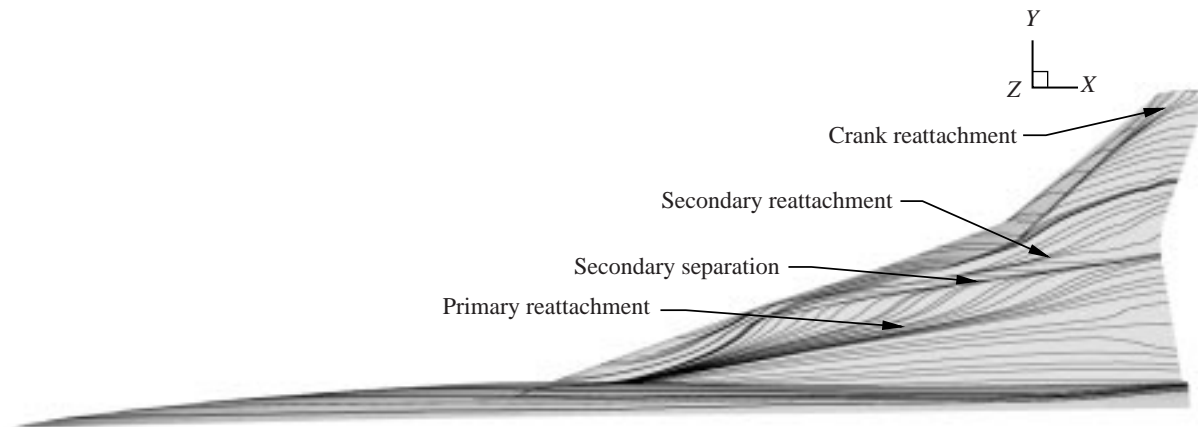
Figure 22. Lower surface pressure coefficients for TCA configuration at $\alpha = 8^\circ$, $M_\infty = 0.24$, and $Re_L = 1.4 \times 10^5$ per inch.



(a) Free air.



(b) Post support.



(c) Post support and wind-tunnel walls.

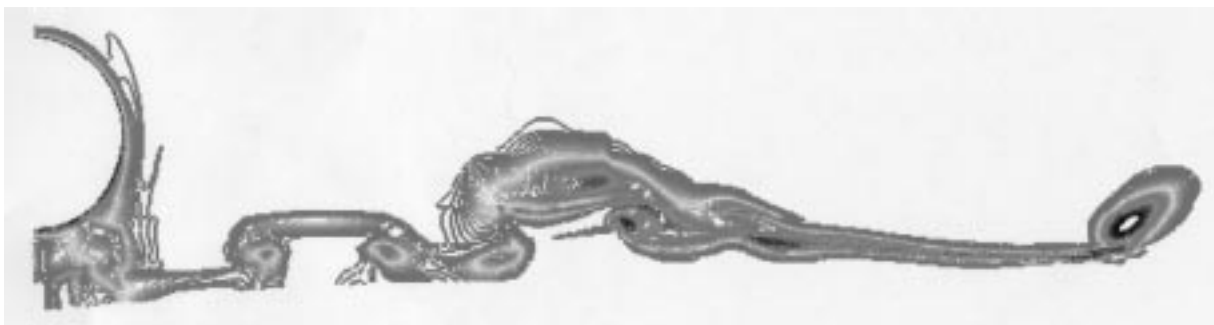
Figure 23. Upper surface streamlines depicted for free air, post support, and post support with wind-tunnel walls at $\alpha = 8^\circ$, $M_\infty = 0.24$, and $Re_L = 1.4 \times 10^5$ per inch.



(a) Free-air.



(b) Post support.



(c) Post support and wind-tunnel walls.

Figure 24. Total pressure contours in near-wake region (MFS = 143 in.) for all three cases viewed from upstream positions at $\alpha = 8^\circ$, $M_\infty = 0.24$, and $Re_L = 1.4 \times 10^5$ per inch.

REPORT DOCUMENTATION PAGE			Form Approved OMB No. 0704-0188	
Public reporting burden for this collection of information is estimated to average 1 hour per response, including the time for reviewing instructions, searching existing data sources, gathering and maintaining the data needed, and completing and reviewing the collection of information. Send comments regarding this burden estimate or any other aspect of this collection of information, including suggestions for reducing this burden, to Washington Headquarters Services, Directorate for Information Operations and Reports, 1215 Jefferson Davis Highway, Suite 1204, Arlington, VA 22202-4302, and to the Office of Management and Budget, Paperwork Reduction Project (0704-0188), Washington, DC 20503.				
1. AGENCY USE ONLY (Leave blank)	2. REPORT DATE November 2000	3. REPORT TYPE AND DATES COVERED Technical Publication		
4. TITLE AND SUBTITLE Analysis of Post-Support and Wind-Tunnel Wall Interference on Flow Field About Subsonic High-Lift High-Speed Research Configuration		5. FUNDING NUMBERS WU 537-07-51-02		
6. AUTHOR(S) Wendy B. Lessard				
7. PERFORMING ORGANIZATION NAME(S) AND ADDRESS(ES) NASA Langley Research Center Hampton, VA 23681-2199		8. PERFORMING ORGANIZATION REPORT NUMBER L-17806		
9. SPONSORING/MONITORING AGENCY NAME(S) AND ADDRESS(ES) National Aeronautics and Space Administration Washington, DC 20546-0001		10. SPONSORING/MONITORING AGENCY REPORT NUMBER NASA/TP-2000-210555		
11. SUPPLEMENTARY NOTES				
12a. DISTRIBUTION/AVAILABILITY STATEMENT Unclassified-Unlimited Subject Category 02 Availability: NASA CASI (301) 621-0390		12b. DISTRIBUTION CODE Distribution: Standard		
13. ABSTRACT (Maximum 200 words) The present study was performed to determine how significant the interference effects of the wind-tunnel model support system and tunnel walls can be for a high-speed configuration during takeoff and landing conditions. A 5-percent scale model of the Technology Concept Airplane was recently tested in the Langley 14- by 22-Foot Subsonic Tunnel. The model was numerically modeled with and without the support and tunnel walls and compared with experimental data. Detailed analysis of the flow provided additional insight concerning what effects the post support and tunnel walls had on the flow field. This study revealed that although the overall forces and moments could be experimentally accounted for, the detailed flow features, such as the surface pressure distributions, could not be accurately simulated without including the post support in the computations.				
14. SUBJECT TERMS Computational fluid dynamics (CFD); High-Speed Research (HSR) Configuration; Technology Concept Airplane (TCA); Subsonic flow; High lift; Model support interference			15. NUMBER OF PAGES 45	
			16. PRICE CODE A03	
17. SECURITY CLASSIFICATION OF REPORT Unclassified	18. SECURITY CLASSIFICATION OF THIS PAGE Unclassified	19. SECURITY CLASSIFICATION OF ABSTRACT Unclassified	20. LIMITATION OF ABSTRACT UL	